Research Square

Preprints are preliminary reports that have not undergone peer review.
They should not be considered conclusive, used to inform clinical practice,
or referenced by the media as validated information.

Effect of Nb concentration on the oxidation behavior of Zr-Nb alloys

Sean Li
Georgia Institute of Technology
Chaitanya S. Deo
Georgia Institute of Technology
Remi Dingreville
Sandia National Laboratories
Scott Monismith
Sandia National Laboratories
Preet M. Singh
preet.singh@mse.gatech.edu

Georgia Institute of Technology

Research Article

Keywords: Zirconium-niobium alloys, High-temperature oxidation, Oxidation kinetics, Steam oxidation, Oxide scales

Posted Date: November 25th, 2026

DOI: https://doi.org/10.21203/rs.3.rs-11678915/v1

License: This work is licensed under a Creative Commons Attribution 4.0 International License.
Read Full License

Additional Declarations: No competing interests reported.

Effect of Nb concentration on the oxidation behavior of Zr-Nb alloys

Sean Li[#], Chaitanya S. Deo*, Remi Dingreville[☆], Scott Monismith[☆], Preet M. Singh[#]

*George W. Woodruff School of Mechanical Engineering (NRE); [#]School of Materials Science and Engineering, Georgia Institute of Technology, Atlanta, GA, US 30332
[☆]Sandia National Laboratories, Albuquerque, NM, US 87123

Corresponding author: Preet M. Singh
Email: preet.singh@mse.gatech.edu

Keywords: Zirconium-niobium alloys; High-temperature oxidation; Oxidation kinetics; Steam oxidation; Oxide scales

Abstract

The oxidation behavior of binary Zr-Nb alloys (pure Zr, Zr-5Nb, Zr-9Nb, and Zr-18.7Nb) was investigated at intermediate temperatures (300°C-500°C) in both dry air and steam environments. By combining thermogravimetric analysis with X-ray diffraction (XRD), scanning electron microscopy (SEM), and energy-dispersive X-ray spectroscopy (EDS), we identified how alloy composition and exposure environment govern early-stage degradation mechanisms. In dry air, pure Zr exhibited rapid, non-protective oxidation driven by grain-boundary diffusion. Adding minor amounts of Nb initially increased the activation energy from 124.6 kJ/mol to 242.0 kJ/mol (Zr-5Nb) due to the suppression of oxygen vacancies. However, metastable hypoeutectoid compositions (Zr-9Nb) suffered from severe phase instability and oxide microcracking. The eutectoid Zr-18.7Nb alloy demonstrated superior oxidation resistance in both environments, achieving sub-parabolic steady-state kinetics (n_2<0.3) through the formation of a dense, chemically stable $Nb_{0.8}Zr_{0.2}O_{2.1}$ mixed-oxide layer that effectively provided a better oxidation resistance under tested conditions. Furthermore, testing in steam revealed a competing environmental effect: while formation of dense scale dramatically reduced the oxidation rate of pure Zr by a factor of 18 compared to air; steam exposure destabilized the intermediate Nb alloys via the precipitation of hydride phases (ZrH_3, NbH_2). These hydrides induced local volumetric expansion that

counteracted the densification benefit. These findings clarify the complex, environment-dependent role of niobium in Zr-Nb binary alloys.

1. Introduction

The oxidation behavior of binary alloys and the composition of oxide formed on the surface depends on the alloy composition, thermodynamic tendency of alloying elements to react in the environment, stability of reaction product (oxide scale in oxygen containing environment), solubility of alloying elements, miscibility of oxides, and the diffusion coefficients of alloying components or oxygen in the oxides. The oxidation behavior of binary alloys is usually investigated in the dilute regime where one element is the primary component while the other is the alloying element. With recent interest in multiple principal component alloys, understanding oxidation behavior over a wider composition range is of interest. In this study, we considered the Zr-Nb alloy system where both Zr rich and Nb rich alloys have been commercially used. However, oxidation behavior of Zr-Nb alloys over a wider range of composition has not been systematically studied.

Zirconium-based (Zr-based) alloys are widely used in the nuclear industry as well as in chemical processing industry due to their excellent corrosion resistance in a variety of environments. Zirconium-based alloys have long been the material of choice for nuclear fuel cladding because of their unique combination of properties, including a low neutron absorption cross-section, mechanical robustness under irradiation, and resistance to corrosion in water and steam environments [1,2].

Zr-Nb alloys were selected for this study as Nb has been a key addition in modern Zr alloys for nuclear industry applications, as it has been associated with improved corrosion resistance and modified oxide growth kinetics [3]. Nb is also known to affect the stability of secondary phase particles and the chemistry of oxide scales, which in turn influences long-term performance. Despite its importance, the role of Nb in the oxidation of Zr alloys over a wider range of composition is not fully understood. While zirconium alloys are the industry standard for LWR (Light Water Reactor) fuel cladding due to their neutron economy and steady-state corrosion they typically contain less than 5% Nb [3, 4]. It is important to understand how the addition of Nb alters the defect chemistry and phase stability of the oxide scale which ultimately determines the long-term protection of alloy.

The specific types of oxides formed and how the oxidation rate transitions over time for a given Zr alloy depends heavily on the environment, whether the environment is air or contains steam. For example, in steam environments, the primary reaction product for Zr has been reported to be monoclinic and tetragonal ZrO_2, accompanied by hydrogen generation [4]. In contrast, nitrogen from air ingress is far from inert at high temperatures and react with Zr. Research by Steinbrück et al. [5] shows that within the temperature range of 600°C to 1200°C, nitrogen penetrates the oxide and reacts to form zirconium nitride (ZrN) near the metal interface. When this intermediate ZrN layer subsequently re-oxidizes, it undergoes a massive volume expansion. This expansion may physically crack the protective scale open, causing a measurable shift in the oxidation kinetics, forcing the slow parabolic growth to abruptly transition into a rapid, linear rate. This phenomenon, known as breakaway oxidation [6, 7], highlights how even small amounts of nitrogen can severely degrade the structural integrity of the cladding [3].

This complexity becomes very obvious when reviewing previous research on Zr alloys with low concentrations of Nb. For instance, Elshanshoury et al. [8] investigated a Zr-1% Nb alloy between 400°C and 700°C and found that the testing atmosphere completely changes both the kinetic stages and the underlying transport mechanisms. Unlike the typical two-stage oxidation behavior of pure Zr, they observed a distinct three-stage corrosion process in pressurized steam. Microstructural analysis of the steam-exposed scales revealed the formation of localized, brain-like oxide structures and blade-like oxide crystals protruding from the surface. Since pure Zr oxidation is dominated by the inward diffusion of oxygen ions via anion vacancies, the growth of these surface protrusions led Elshanshoury et al. to propose a model where zirconium cation diffusion through cation vacancies to the surface also plays a critical role under steam environments [8]. Furthermore, regarding the effect of Nb additions on the degradation rate, the outcome is highly dependent on the testing atmosphere. While moderate Nb addition reduces oxygen vacancy concentration and slows down oxidation in dry air via the doping effect, it acts as a destabilizer in steam environments. In pressurized steam, pure Zr exhibits superior intrinsic resistance due to a steam-induced scale densification effect. Conversely, Nb-containing alloys suffer from accelerated corrosion in steam due to the precipitation of hydride phases (such as ZrH_3 and NbH_2), which generate localized volumetric expansion and microcracking, thereby disrupting

the protective oxide barrier. On the other hand, Roy et al. [9] tested alloys in dry air and suggested that adding Nb actually improves oxidation resistance. Even at slightly higher concentrations, the trend is not straightforward; Arima et al. [10] examined Zr-10 wt.% Nb in air and reported a non-linear relationship between Nb content and the oxidation rate. Because these prior studies mostly concentrated on low-to-moderate niobium compositions (typically <10 wt.% Nb) across entirely different testing environments, their collective conclusions on the effect of Nb addition on corrosion behavior of Zr-alloys remain contradictory. This observed variability is intrinsically linked to the dual role of niobium within the oxide scale, affecting both phase stability and protection mechanisms. As Commercial alloys like M5® (~1 wt.% Nb) demonstrate, maintaining the β-Nb phase is crucial for corrosion resistance [11, 12]. However, as detailed by Otgonbaatar et al. [13], Nb also acts as a dopant within the tetragonal ZrO_2 layer. When pentavalent Nb (Nb^{5+}) substitutes for tetravalent Zr (Zr^{4+}) in tetragonal ZrO_2 under oxygen-rich conditions, the resulting positive effective charge is compensated by an increase in negatively charged Zr vacancies, accompanied by a decrease in oxygen vacancy concentration [13], the lattice must maintain electroneutrality by consuming pre-existing oxygen vacancies as shown in Equation (1):

$$Nb_2O_5 + V_O^{\cdot\cdot} \xrightarrow{ZrO_2} 2Nb_{Zr}^{\cdot} + 5O_O^{\times} \qquad (1)$$

Otgonbaatar et al. [13] predicted that, within a dilute-defect thermodynamic model at 1500 K and an oxygen partial pressure of 1 atm, Nb incorporation into tetragonal ZrO_2 reduces the oxygen vacancy concentration by approximately 80% relative to undoped ZrO_2. This massive reduction directly lowers the oxygen self-diffusivity by 80% as well. Because oxygen vacancies act as the primary diffusing species, this quantitative drop fundamentally explains the slower parabolic growth rates observed in our experiments. It is worth noting, however, that Nb doping also elevates the concentration of Zr vacancies (by roughly 60 times) and increases free electrons. If the local Nb content becomes excessive, this enhanced electron transport can overcome the benefit of reduced oxygen vacancies and ultimately accelerate oxidation.

Therefore, the contradictory role of Nb in Zr-alloy corrosion in literature is likely a result of differences in the environments in which these alloys were tested. While individual behaviors in air [3] or steam [14] are documented, a direct, systematic

comparison of high-Nb binary alloys across these two environments is lacking. Specifically, the transition in oxidation mechanism as the alloy composition crosses the solubility limit into the two-phase (α + β) region remains poorly defined. This work addresses these gaps by providing a direct comparison of kinetics and oxide morphology for hypoeutectoid Zr-Nb alloys in both air and steam-containing environments.

2. Experimental

2.1 Sample preparation

Four alloys, with hypoeutectoid and eutectoid compositions based on the Zr-Nb phase diagram, shown in Figure 1, were tested in this study. Samples included a 100% Zr and three binary Zr-Nb alloys of different compositions: 5% Nb, 9% Nb, 18.7% Nb. Each alloy composition was homogeneously melted in electric arc furnace, Centorr Vacuum Industries' Model 5BJ equipped with a water-cooled copper hearth and a tungsten electrode. Pure Zirconium (~ 99.9 wt.% from American Elements) and pure niobium (~99.9 wt.% from American Elements) pellets were used to prepare the alloys for this study. To ensure a clean melting environment, the chamber was evacuated and backfilled with high-purity argon five times. Each ingot was remelted and flipped ten times to ensure chemical homogeneity [15]. The final alloy ingots were cut into test samples by using IsoMet™ 4000 Linear Precision Saw. Alloys were formulated to represent key hypoeutectoid and eutectoid compositions along the binary Zr-Nb phase diagram, as shown in Figure 1.

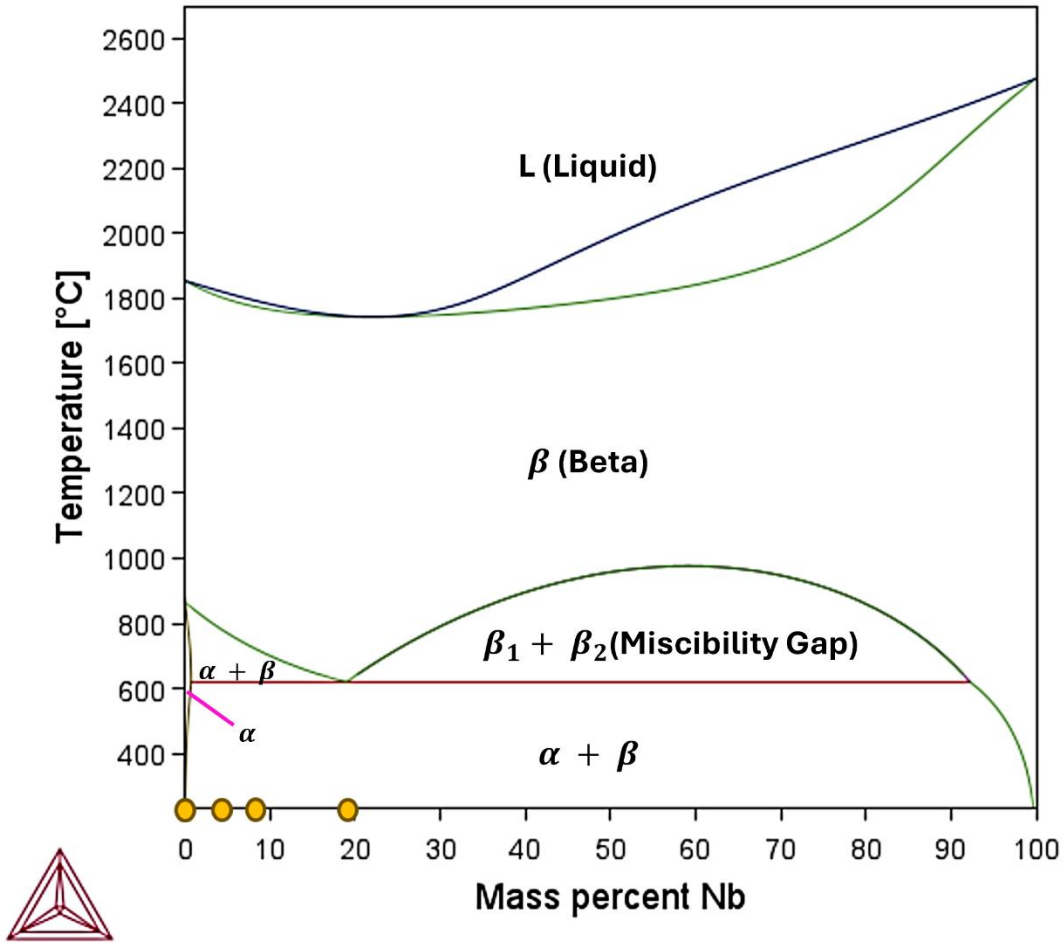

Fig. 1 Binary phase diagram of Zr-Nb alloy (Mass percent Nb) [16]. Points on the x-axis show the alloy compositions tested in this study.

2.2 Oxidation Tests

Oxidation tests in air atmosphere were conducted using a D-100 Cahn Thermobalance with a tube furnace. The micro-balance is capable of detecting weight changes due to oxidation as small as 1 microgram. Tests were conducted in the range of 300°C to 500°C for 120 hours. Flow rate of air was maintained at 110 SCCM throughout each test. Weight gain as a function of time was recorded to determine the oxidation kinetics under each condition.

For comparison, the oxidation tests in steam atmosphere were conducted using a tube furnace over a temperature range of 300°C to 500°C for 1 day, 2 days, 7 days, and 15 days. Steam was generated in a separate chamber and introduced into the test chamber along with the air as a carrier gas. Flow rate of steam as well as air was maintained at

100 SCCM each. Tested samples were removed from the furnace after test duration and further characterized.

After each oxidation test was completed, samples were allowed to cool down and were removed from the furnace carefully to avoid any scale spallation. Samples were stored in air-tight containers for further characterization. For the samples tested in steam-containing environment, the weight gain due to oxidation in steam atmosphere was measured by analytical balance with accuracy of 0.0001g, which was also used for the initial weight of these samples.

2.3 Microstructural Characterization of base alloy

To identify the constituent phases and assess their stability in the as-received and oxidized alloys, X-ray diffraction (XRD) analysis was performed. XRD scans were conducted to determine the crystal structures present in the bulk alloy and the oxide scales, specifically focusing on the detection of monoclinic and tetragonal ZrO_2 phases as well as Nb-rich precipitates.

For microstructural analysis, standard metallographic methods were employed. Phases present in the base alloys were determined by XRD analysis. After that the samples were mounted in epoxy, ground to expose the cross section of sample and oxide, and polished to a mirror finish. Chemical etching was subsequently applied to reveal the grain boundaries, phase distribution, and oxide scale morphology. The microstructure was then examined using optical microscopy and Scanning Electron Microscopy (SEM).

2.4 Post Oxidation Characterization

Tested samples were further characterized for the composition and morphology of oxides formed at their surface. Post-test characterization for samples tested in air or in the steam-containing environment was similar. First, the XRD analysis of surface oxides was carried out using Rigaku Smartlab XE XRD for phase identification. After that, the tested samples were edge-mounted in epoxy, ground to reveal the oxide cross section, polished and coated with gold for better conductivity for SEM imaging by using Hummer 6 Sputterer - Gold Target. All mounted samples were examined for oxide morphology and composition by using a scanning electron microscope (SEM) equipped with Energy-dispersive X-ray spectroscopy (EDS). Zeiss Ultra60 FE-SEM as well as

Hitachi SU8230 SEM were used to examine the oxidized samples.

3. Results

3.1 Oxidation Behavior in Air

The air-oxidation behavior of the Zr-Nb alloys (100% Zr, Zr - 5% Nb, Zr - 9% Nb, Zr -18.7% Nb) in air at 300°C, 400°C, and 500°C is shown in Figures 2 (a) to 2 (d). These figures show the weight gain per unit area (ΔW/A) as a function of exposure time (t). As expected, the rate of oxidation increases with an increase in test temperature for all tested alloys. These oxidation curves reveal two distinct kinetic regimes: an initial transient stage characterized by rapid increase in the weight by oxygen uptake, followed by a later steady-state oxidation stage where the growth rate typically decreases or stabilizes, depending on the alloy composition and temperature.

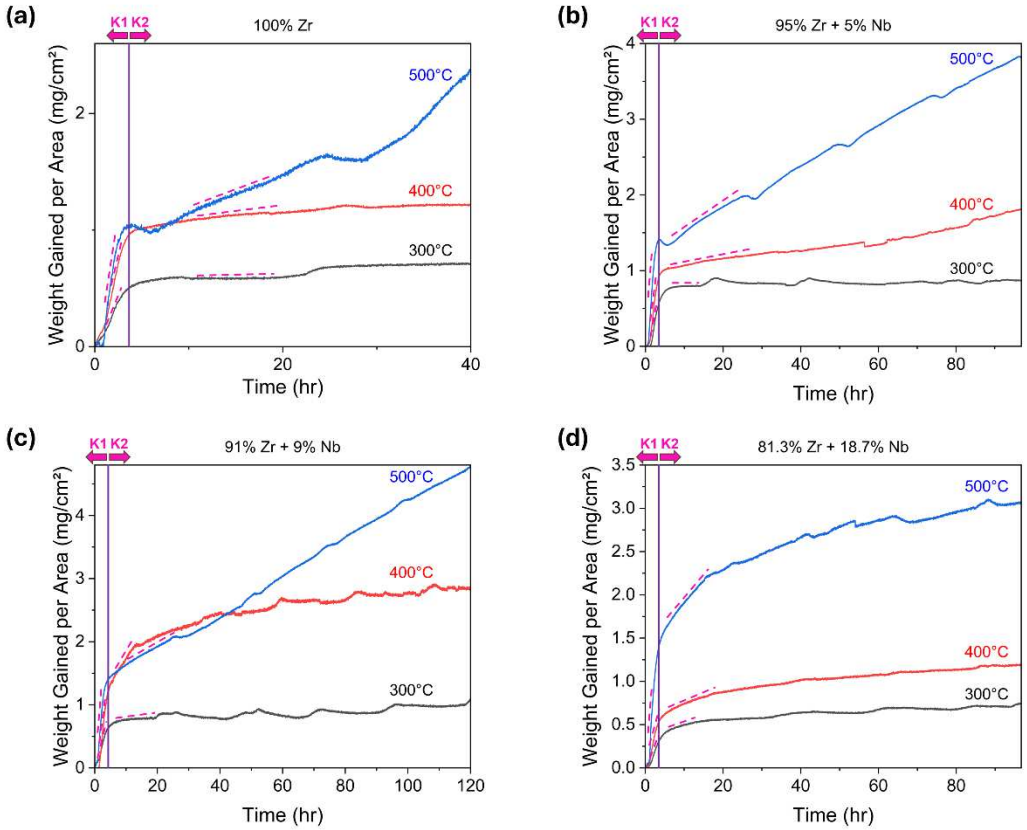

Fig. 2 TGA curves for (a) pure Zr, (b) Zr–5% Nb, (c) Zr–9% Nb, and (d) Zr–18.7% Nb during oxidation in dry air at three temperatures between 300 and 500 °C.

3.2 Identification of the Kinetic Transition (Inflection Point)

The change in the oxidation rate was used to quantify the time when the oxidation rate decreases after rapid initial oxidation under each tested condition. This inflection point in kinetic curves was determined by plotting the oxidation rate (weight gain / unit area / time) versus time, as illustrated by representative examples in Figure 3. The curves exhibit an initial increase in the oxidation rate with time, reaching a maximum value defined here as the inflection point, after which the rate of oxidation gradually decreases. Reaching this inflection point indicates the formation of an initial protective oxide scale. The subsequent drop in the oxidation rate is mainly due to a transition from reaction-controlled to diffusion-controlled growth of the oxide scale at the metal surface. This decrease in oxidation rate likely occurs because the initially formed oxide scale acts as a physical barrier, increasing the diffusion path length for oxygen as described by Wagner's theory [6]. Therefore, identifying these inflection points helps assess when each alloy begins to passivate.

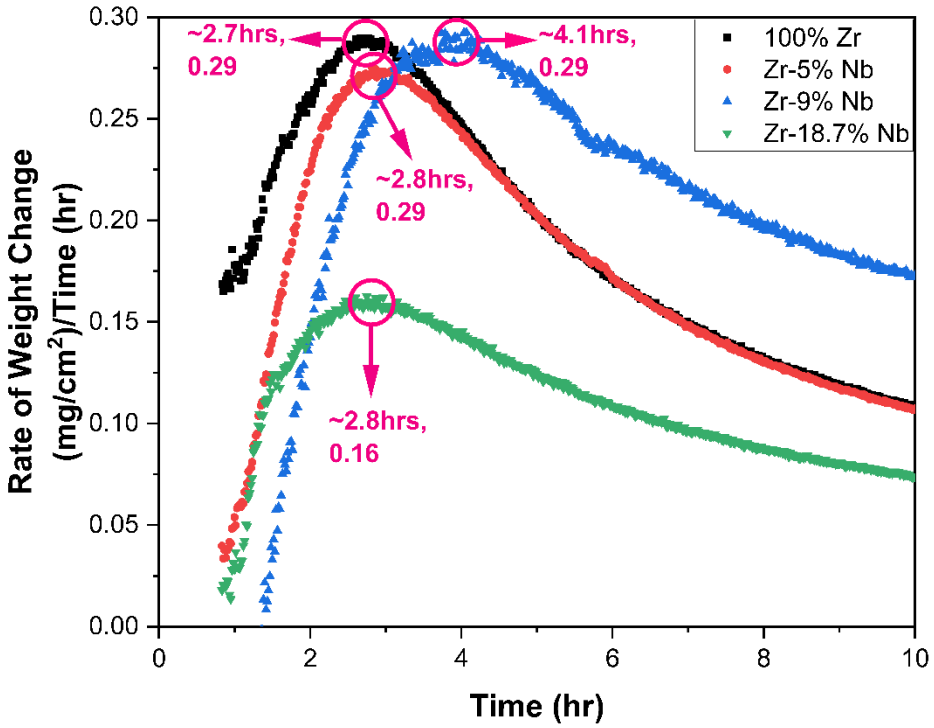

Fig. 3 Rate of weight change vs time plot showing an inflection point for 100% Zr, Zr-5% Nb, Zr-9% Nb, and Zr-18.7% Nb alloys tested at 400°C in air.

3.3 Determination of Kinetic Parameters (n and K) via Log-Log Analysis

Based on the identified inflection points, the oxidation data for each alloy was divided into Region 1 (Initial Stage) and Region 2 (Later Stage). The oxidation kinetics were analyzed using the general power-law equation using Equation 2:

$$\frac{\Delta W}{A} = Kt^n \qquad (2)$$

where ΔW/A is the mass gain per unit area (mg cm^{-2}), t is the exposure time (h), K is the fitted rate constant, and n is the kinetic exponent. With these units, K has units of mg cm^{-2} h^{-n}.

Taking the base-10 logarithm of both sides of Equation 2 gives:

$$\log_{10}\left(\frac{\Delta W}{A}\right) = \log_{10} K + n \log_{10} t \qquad (3)$$

For each region, n was obtained from the slope of the corresponding log-log fit. The intercept gives $\log_{10}K$, and K was obtained by taking the base-10 antilogarithm of the intercept. The fitted parameters are denoted by K_1 and n_1 for Region 1 and by K_2 and n_2 for Region 2. An exponent near 1 indicates approximately linear mass-gain kinetics, whereas an exponent near 0.5 indicates approximately parabolic kinetics. Values between 0 and 0.5 indicate sub-parabolic power-law behavior. These exponents describe the measured kinetic behavior; the underlying transport mechanisms are interpreted together with the microstructural observations.

For instance, the formation of complex defect structures or protective thin films can shift the oxidation kinetics toward sub-parabolic regimes, such as logarithmic or cubic growth (e.g., Zr-18.7% Nb, as shown in Figure 4 (b)).

To assess this long-term passivation capability, we determined the steady-state kinetic exponent (n_2) for Region 2. Linear regression was restricted to the stable portions of the log-log plots post-inflection, deliberately excluding the initial transient stage (Region 1) to isolate the actual diffusion-controlled mechanisms.

The experimental data demonstrate the following composition-driven theoretical deviations. Pure Zr failed to form a stable scale in the region 2, resulting in a porous, microcracked structure, as shown in Figure 5 (a) with poor protection. However, adding a small amount of Nb offered slight improvement: the hypoeutectoid Zr-5Nb alloy

prevented macroscopic delamination but still exhibited outer surface porosity, as shown in Figure 5 (b). Increasing the Nb content to the metastable Zr-9Nb composition reintroduced structural instability and irregular scale thickening, as shown in Figure 5 (c). In contrast, the eutectoid Zr-18.7Nb alloy formed a compact, adherent mixed-oxide layer with optimized grain boundaries shown in Figure 5 (d). This dense structure effectively restricted standard Wagner-type diffusion, leading to a highly protective sub-parabolic growth stage (n_2<0.3, as shown in Figure 4 (b)) and preventing the internal stress cracking observed in the unstable alloys.

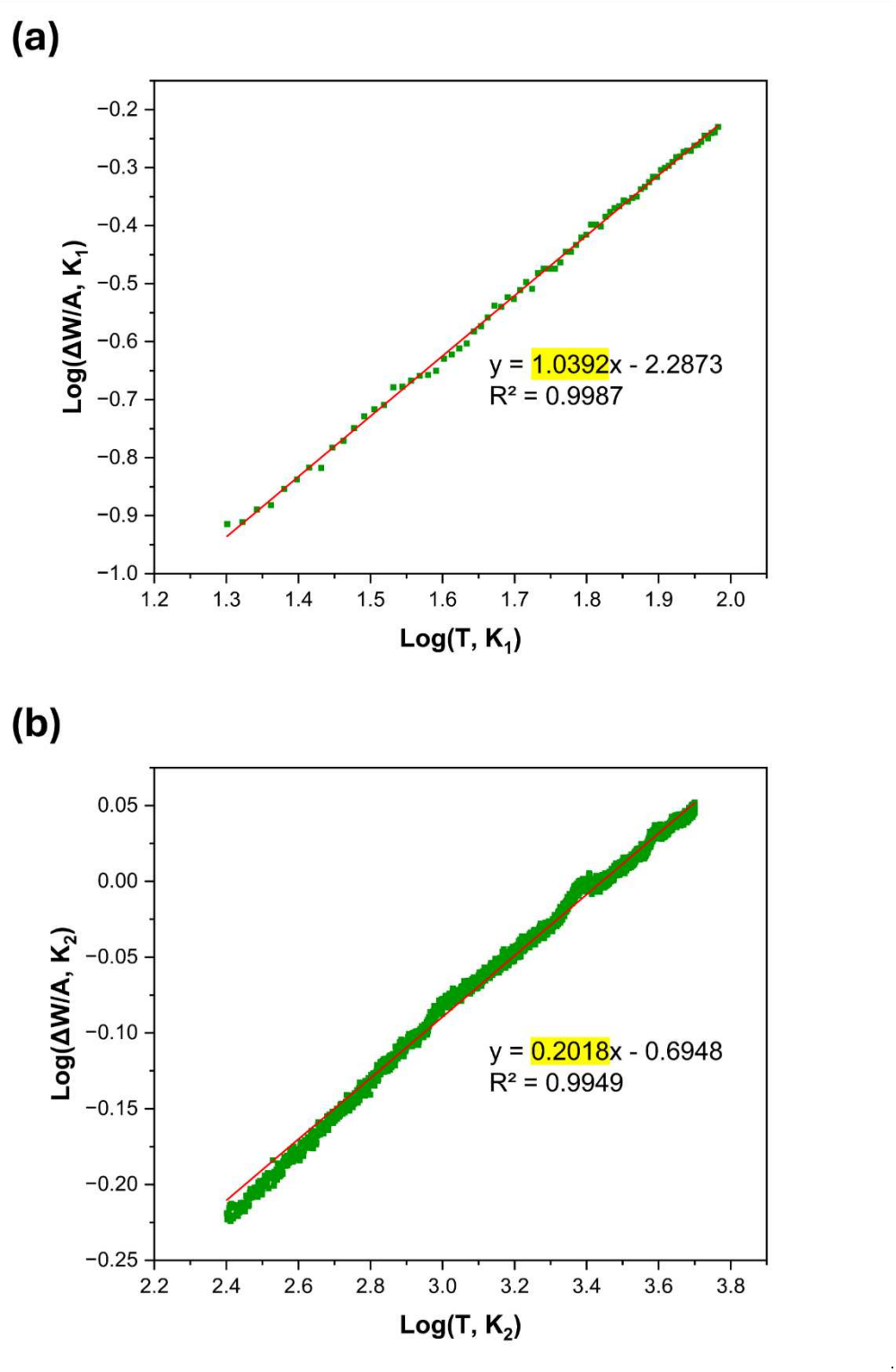

Fig. 4 (a) Log-log plot of the initial oxidation kinetics (Region 1) for the 100% Zr alloy oxidized at 400°C in dry air for 5 days, (b) Log-log plot of the later oxidation kinetics (Region 2) for the Zr-18.7% Nb alloy oxidized at 400°C in dry air for 5 days. The linear fit and the corresponding equation used to determine the rate constant (K) and kinetic exponent (n) are shown.

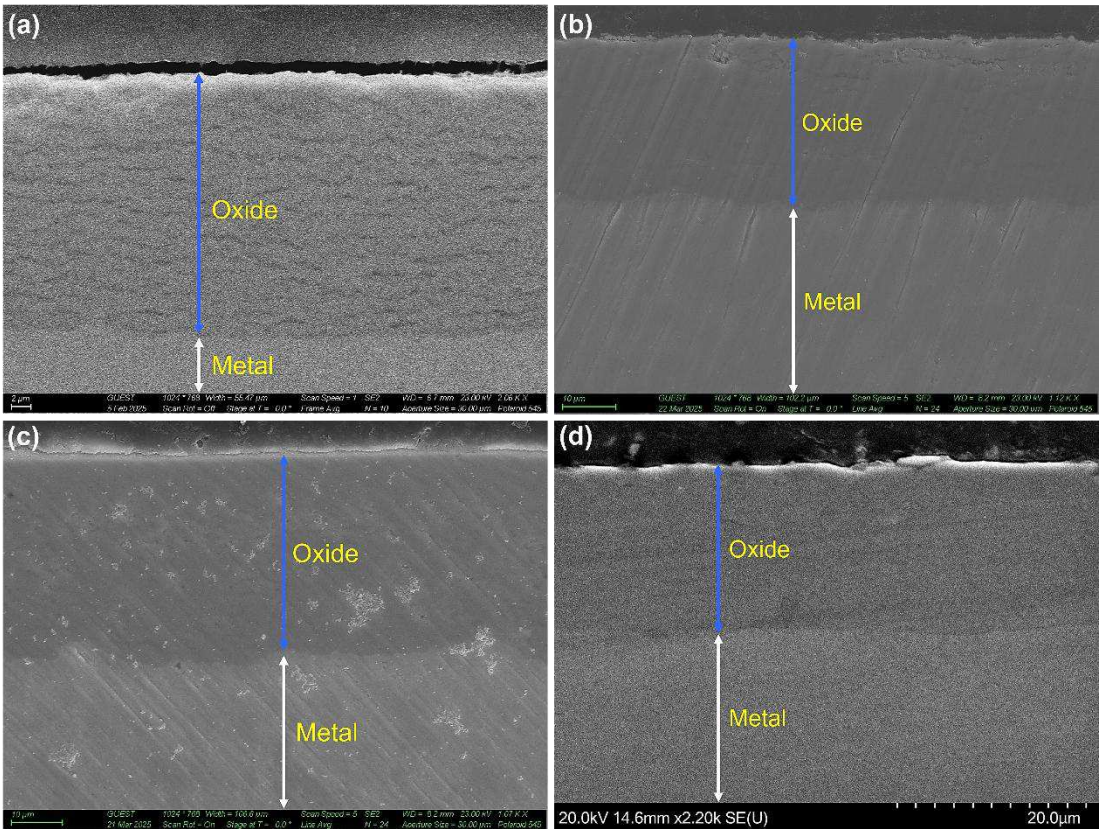

Fig. 5 SEM Micrograph of oxide formed on (a) 100% Zr, (b) Zr-5% Nb, (c) Zr-9% Nb, (d) Zr-18.7% Nb alloy samples exposed to air environment at 500ºC for 120 hours.

Table 1. Summary of K_1, K_2, n_1 and n_2 values for Zr-*x*Nb alloys from 300°C to 500°C.

Alloy (wt.%)	**Pure Zr**	**Zr-5Nb**	**Zr-9Nb**	**Zr-18.7Nb**
K_1 (300°C)	1.01×10^{-3}	2.39×10^{-5}	8.69×10^{-5}	6.95×10^{-4}
n_1 (300°C)	1.22	2.02	1.72	1.22
K_2(300°C)	0.27	0.61	0.24	0.19
n_2 (300°C)	0.11	0.04	0.15	0.15
K_1 (400°C)	5.16×10^{-3}	9.69×10^{-4}	1.71×10^{-3}	0.01
n_1 (400°C)	1.04	1.42	1.27	0.78
K_2 (400°C)	0.46	0.49	0.53	0.2
n_2 (400°C)	0.11	0.12	0.2	0.2

K_1 (500°C)	0.03	0.02	0.02	0.02
n_1 (500°C)	0.75	0.92	0.9	0.94
K_2 (500°C)	4.48×10^{-3}	0.06	0.1	0.51
n_2 (500°C)	0.81	0.46	0.42	0.21

3.4 Activation Energy Calculation for the Initial Oxidation Stage (Region 1)

To quantify the energy barrier for initial oxidation stage, the Region 1, of oxidation curves, the activation energy (Q) was calculated using the Arrhenius relationship.

The Arrhenius equation is expressed as Equation 4:

$$K = K_0 \cdot \exp\left(-\frac{Q}{RT}\right) \qquad (4)$$

Linearizing this equation gives Equation 5:

$$\ln(K) = \ln(K_0) - \frac{Q}{R}\left(\frac{1}{T}\right) \qquad (5)$$

Raw estimation of activation energy (Q) for Initial oxidation region was ≈ 27.0 kJ/mol for 100% Zr sample tested in air, as shown in Figure 6 (a).

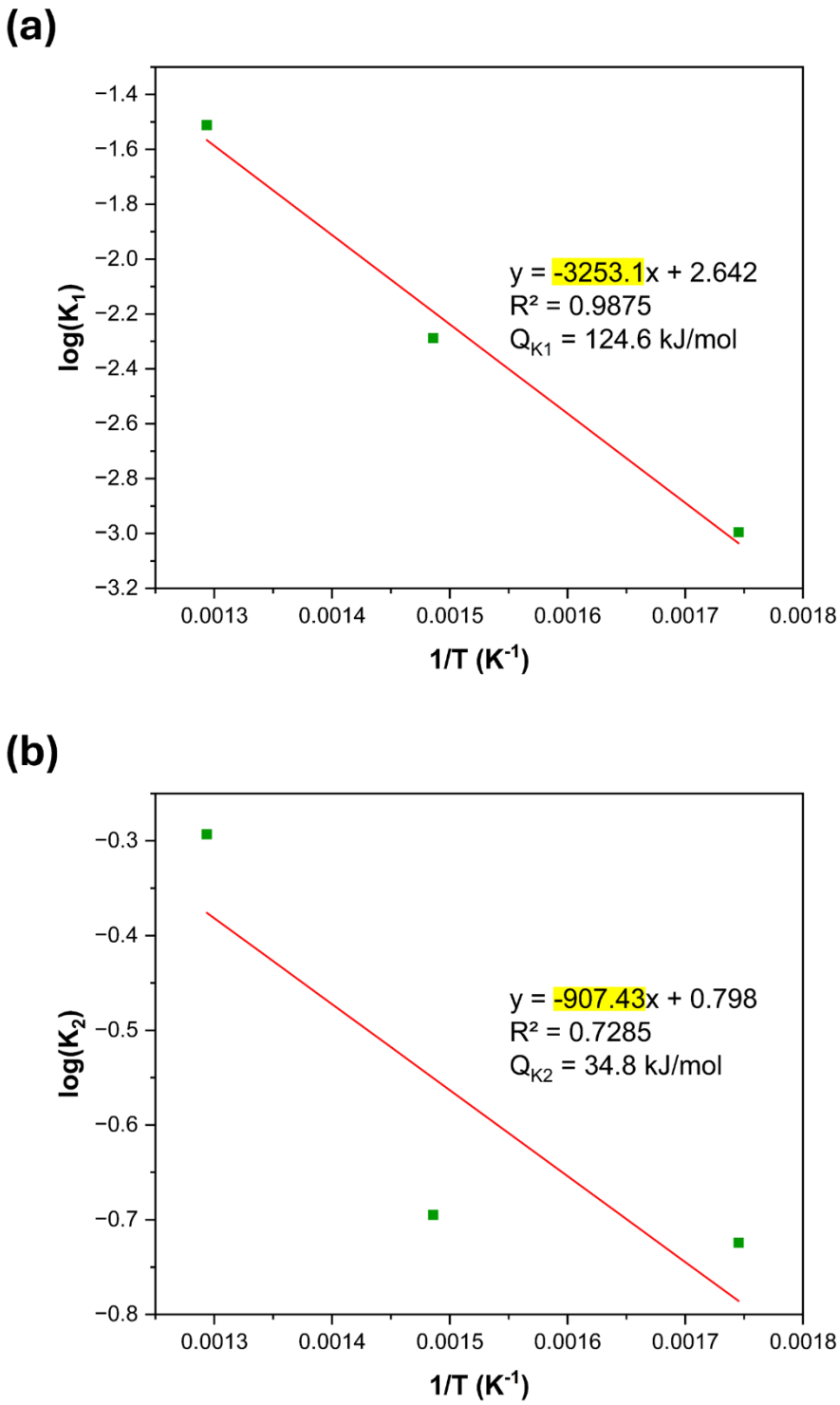

Fig. 6 Arrhenius plots of (a) log(K_1) versus 1/T for the initial oxidation stage (Region 1) of pure Zr and (b) log(K_2) versus 1/T for the later oxidation stage (Region 2) of Zr–18.7% Nb during oxidation in dry air at 300–500 °C for 5 days. Linear fits and their corresponding equations are shown for determining the apparent activation energies, QK_1 and QK_2, respectively.

The activation energy (Q) reported in this study was calculated for oxidation data from the 300°C to 500°C isotherms. Following Equation (2) ~ Equation (5), the activation energy for pure Zr was determined to be 124.6 kJ/mol. This value aligns with the activation energy for vacancy migration in zirconia (~28-31 kcal/mol or 117-130 kJ/mol), as discussed by Madeyski and Smeltzer [17], suggesting that the transport is dominated by short-circuit paths where defect formation energy is negligible. Similarly, activation energy values for initial oxidation region, Region 1, were determined for all four alloys tested in this study, as listed in Table 2. Data suggests that the activation energy for initial oxidation increases with 5% Nb addition and then decreases with further addition up to the eutectoid composition.

The fitted kinetic exponents n_1 and n_2 are listed in Table 1, whereas the apparent activation energies QK_1 and QK_2 are summarized in Table 2. These results enable us to correlate the numerical kinetic parameters with the physical degradation mechanisms observed in the microstructure.

In this study, while the initial oxidation regime prior to the inflection point yields well-correlated activation energies (Q_{K1}) for all samples, determining the steady-state activation energy (Q_{K2}) for Region 2 was only mathematically and physically viable for the eutectoid Zr-18.7Nb alloy (Fig. 6 (b)).

We found that using the Arrhenius equation to calculate the activation energy (Q_{K2}) for post-inflection regions of oxidation curves did not show good correlation for Pure Zr, Zr-5Nb, and Zr-9Nb because their oxide scales become structurally unstable, leading to linear corrosion rates. The Arrhenius equation assumes that the oxidation mechanism, and therefore the kinetic exponent (n), stays the same across different temperatures. However, our log-log plots show that the Region 2 exponent (n_2) for these three materials changes with temperature, as summarized in Table 1 (e.g., n_2 increases from 0.11 at 300°C to 0.81 at 500°C for Pure Zr, and from 0.04 to 0.46 for Zr-5Nb). For example, the SEM image in Fig. 7 (c) shows that the Zr-9Nb oxide scale suffers from irregular thickening and internal cracking at higher temperatures. Because the unit of the rate constant (K_2) depends directly on the value of n_2, comparing K_2 values for different oxidation kinetics mechanisms, with different the fitted kinetics relationships, is not appropriate. Because of this, it is impossible to use a single activation energy (Q_{K2}) to describe this later stage.

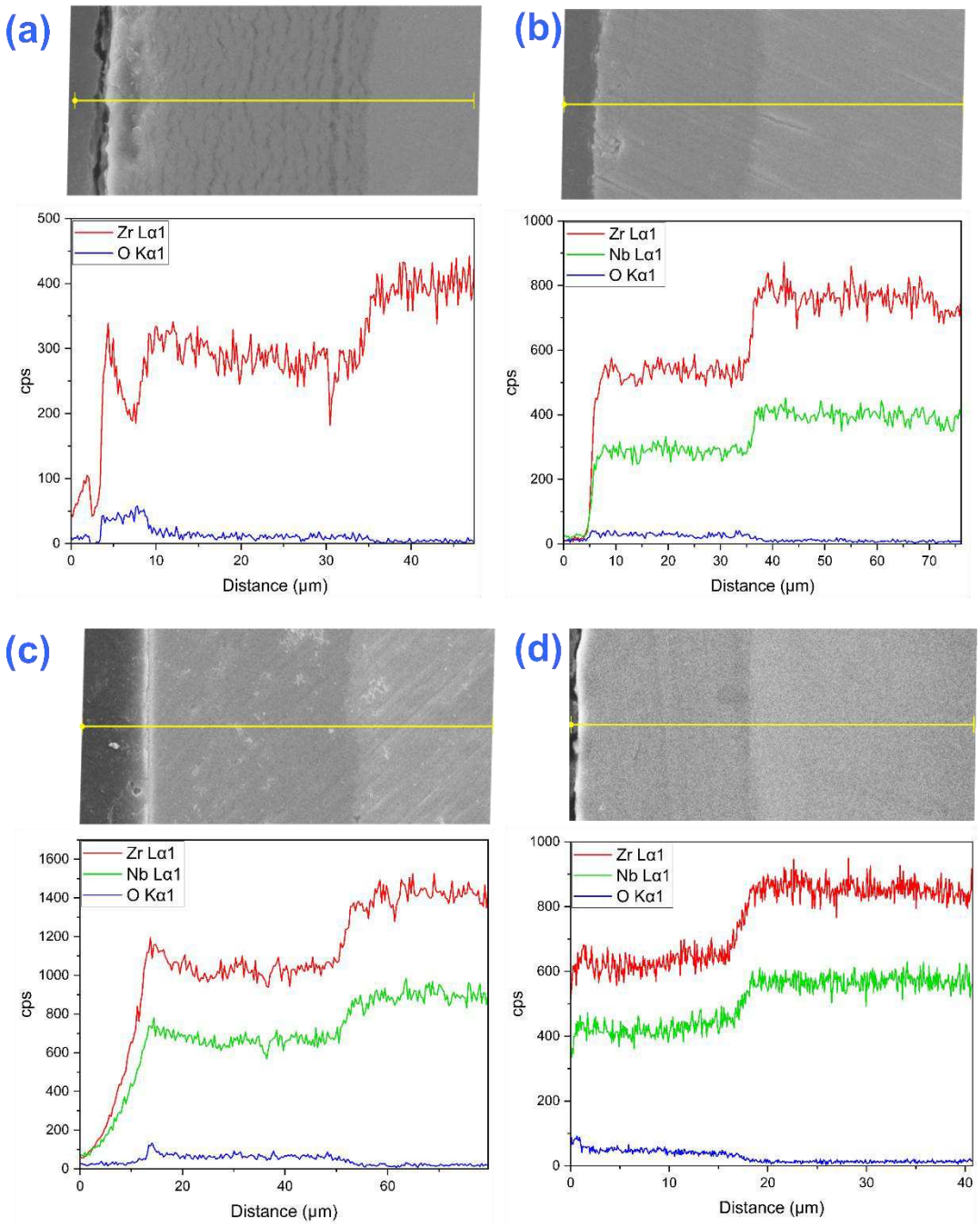

Fig. 7 EDS Line Scan for (a)100% Zr, (b) Zr-5% Nb, (c) Zr-9% Nb, (d) Zr 18.7% Nb alloy samples in air at 500°C for 120 hours.

However, the eutectoid Zr-18.7Nb alloy behaves differently. Since it does not suffer from scale degradation, it follows the Arrhenius relationship well during the steady-state stage. As shown in the log (K_2) vs 1/T plot, we obtained a valid linear regression with a proper negative slope for Zr-18.7Nb. This confirms that its oxidation mechanism stays consistent from 300°C to 500°C. Ultimately, this mathematical validity proves

that the dense mixed-oxide layer effectively prevents structural instability, matching the superior protectiveness we observed in the SEM analysis (Fig. 5 (d)).

Table 2. Comparison of activation energies (Q) for the initial (Region 1) and later (Region 2) stages of Zr-xNb alloys.

Alloy (wt.%)	Pure Zr	Zr-5Nb	Zr-9Nb	Zr-18.7Nb
Q_{K1} (kJ/mol)	124.6	242	191.8	119.7
Q_{K2} (kJ/mol)	-	-	-	34.8

3.5 Grain Boundary Diffusion in Pure Zr

For Pure Zr, the calculated activation energy for initial oxidation in air was 124.6 kJ/mol. Our measured activation energy 124.6 kJ/mol matches the enthalpy of oxygen vacancy migration in monoclinic zirconia (~117–130 kJ/mol) much better than the total bulk diffusion energy (~234 kJ/mol) [17]. Since bulk diffusion also requires energy for vacancy formation (~105–117 kJ/mol) [17], the absence of this formation term in our data implies that pre-existing defects may play a major role in oxidation of Zr under tested conditions. This also suggests that the grain boundary short-circuit diffusion, which requires negligible vacancy formation energy, most likely dominates the oxidation process. The stark contrast of activation energy between Pure Zr (124.6 kJ/mol) and Zr-5Nb (242 kJ/mol) highlights the role of Nb in altering the oxide structure from a coarse-grained monoclinic phase to a more protective passivation film.

Based on the data in Table 2, the activation energy changes depending on the Nb concentration. It first increases from 124.6 kJ/mol for Pure Zr to 242 kJ/mol for Zr-5Nb. This may be explained due to the Doping Effect [13], where the substitution of Nb^{5+} reduces the number of oxygen vacancies required for electroneutrality. With fewer vacancies, oxygen diffusion is restricted, leading to a higher activation energy. With the addition of higher concentration of Nb, the activation energy decreases again, (191.8 kJ/mol for Zr-9Nb and 119.7 kJ/mol for Zr-18.7Nb). For the Zr-9Nb alloy, this drop in initial activation energy (Q_{K1}) may reflect changes in both oxide defect chemistry and microstructural transport pathways. Microstructural heterogeneity associated with the metastable two-phase matrix (α -Zr + β-Zr) may promote short-circuit transport during oxide formation. In addition, Nb-induced increases in Zr vacancy concentration could

facilitate outward Zr diffusion [13]. However, reported activation energies for Zr diffusion in 3 mol.% yttria-stabilized tetragonal zirconia are approximately 515 kJ/mol for lattice diffusion and 370 kJ/mol for grain-boundary diffusion [18], both higher than the measured QK_1 of 191.8 kJ/mol. Although differences in oxide composition, structure, and temperature limit direct comparison, the present data do not establish outward Zr diffusion as the rate-controlling mechanism. During the early stages (Region 1), high localized transformation stresses and phase boundary mismatches promote a high density of sub-microscopic defects and interfacial boundaries at the oxide/metal interface, lowering the energetic barrier for short-circuit oxygen ingress. Although direct SEM observations in Fig. 5 (c) capture the post-test scale (after Region 2), the severe scale fragmentation, irregular thickening, and microcracking observed after prolonged exposure serve as structural evidence of the inherent mechanical instability and persistent stress accumulation that originated during early film formation. Zr-18.7%Nb's activation energy of 119.7 kJ/mol is quite similar to the grain boundary diffusion value in pure monoclinic zirconia.

3.6 Oxidation behavior in steam-containing environment

Oxidation tests in steam-containing environment were performed in a horizontal tube furnace, as described earlier in Section 2.2. The weight change per unit area as a function of time is plotted for each individual alloy across the 300°C-500°C temperature range, as shown in Figures 8 (a) to 8 (d). Overall, most alloys exhibited parabolic oxidation kinetics, but their temperature dependencies varied significantly based on their compositions.

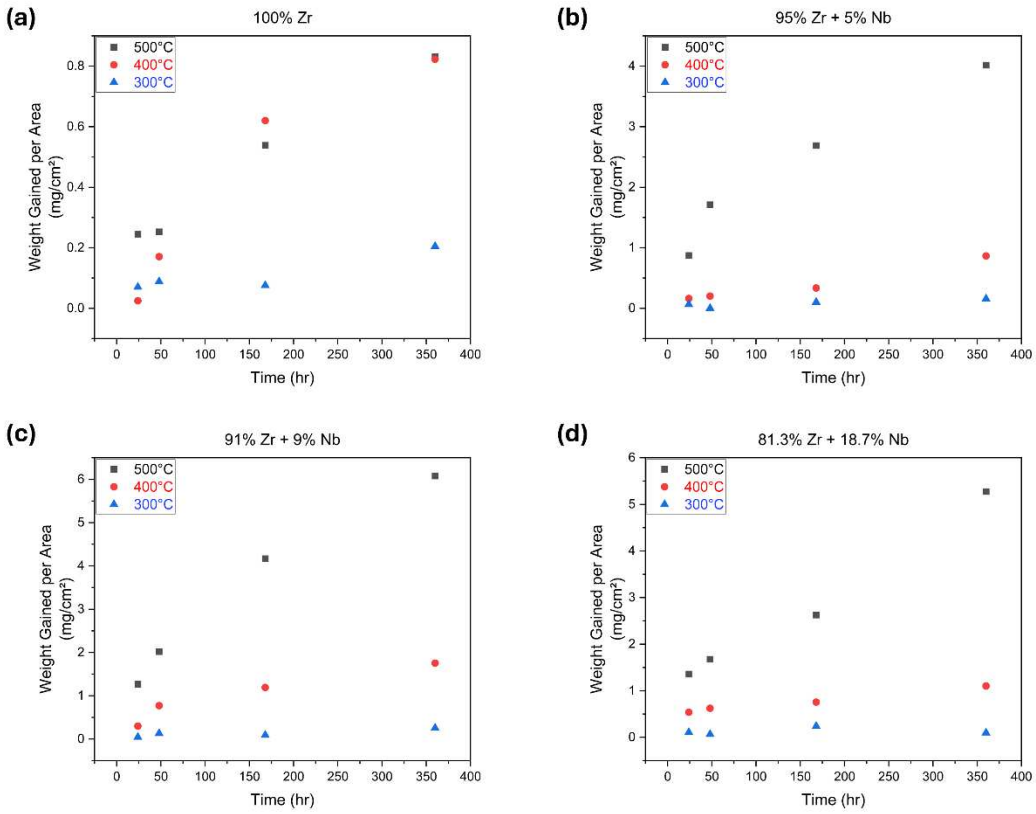

Fig. 8 Mass-gain data for (a) pure Zr, (b) Zr–5% Nb, (c) Zr–9% Nb, and (d) Zr–18.7% Nb tested from 300°C to 500°C in steam-containing environments for 1 day, 2 days, 7 days and 15 days.

Comparing the oxidation results at low-temperatures, the oxidation rates for alloys tested at 300°C in steam-containing environment were lower compared to the equivalent tests done in air. These minimal weight gains at 300°C indicate that the oxides formed in the presence of steam were more protective than the ones formed in air. These results suggest that the oxygen or metal ion transportation through the initial oxide film was lower for the film formed in the presence of steam.

Upon increasing the temperature to 400°C (red circles in Figs. 8 (a) - 8 (d)), a clear separation of material performance in a steam-containing environment begins to emerge. Quantitative comparison of weight gain data demonstrates this divergence. Even when considering the instrumental measurement uncertainty from the analytical balance (±0.0001 g, corresponding to ~0.05 mg/cm²), the absolute weight gain difference between the stable eutectoid alloy (Fig. 8 (d)) and the other three alloys, Pure Zr, Zr-5Nb, and Zr-9Nb (Figs. 8 (a), 8 (b), and 8 (c)), exceeds their respective standard

errors, confirming that the difference in their oxidation rates is meaningful and reflects genuine degradation mechanisms rather than experimental scatter.

The difference in oxidation behavior between the tested alloys in steam-containing environment becomes most apparent at 500°C (black squares in Figs. 8 (a)- 8 (d)). Pure Zr (Fig. 8 (a)) and the hypoeutectoid alloys (Zr-5Nb and Zr-9Nb, Figs. 8 (b) and 8 (c)) showed significantly higher mass gains, pointing to a faster transportation of reactants or a structural breakdown of their oxide scales. On the other hand, the eutectoid Zr-18.7Nb alloy (Fig. 8 (d)) remained stable, showing a nearly flat kinetic curve.

To verify the reliability of the measurements, the standard error (SE) was analyzed. For Zr-18.7% Nb alloy, the variation was calculated to be approximately ±1.3 mg/cm² (at 500°C, 15 days). This shows that the eutectoid alloy leads to protective oxide formation in the presence of steam, effectively preventing the breakaway observed in the other compositions.

3.7 Post Test Characterization: X-Ray Diffraction Results

Oxidation in Air

To understand the overall oxidation behavior of tested metals, a series of oxidation tests were performed where the samples were only oxidized for 1 hour to see how the initial oxide in region-1 was different from the final oxide after 120 hours. This was performed to characterize the oxide formed pre-inflection point, in region-1, and compare with the final oxide after 120-hour exposure.

The oxidized samples were characterized using X-Ray diffraction (XRD). Results in Figure 9 (a) to Figure 9 (d) show the XRD patterns for the untested metal samples, as well as the samples oxidized in air at 500°C after 1 hour of exposure, and after 120 hours of exposure. A critical comparison of these patterns reveals the impact of Niobium. The primary oxidation product of Zr-based alloys was found to be zirconium dioxide (ZrO_2). Depending on temperature and stress conditions, this oxide may exist as monoclinic (m-ZrO_2), cubic (c-ZrO_2) or tetragonal (t-ZrO_2) phases. When Nb is added into pure Zr, Nb becomes incorporated into the oxide, potentially forming separate phases like Nb_2O_5 at higher concentrations.

Figure 9 (a) to Figure 9 (d) also shows the XRD patterns for the respective metal samples before oxidation. According to Figure 9 (a), the 100% Zr sample contains α-phase zirconium, corresponding to a Hexagonal Close-Packed (HCP) crystal structure. Similarly, XRD in Figure 9 (b) shows that the Zr-5% Nb sample mostly contains α-phase zirconium, with two peaks corresponding to β-phase zirconium, which possesses a Body-Centered Cubic (BCC) crystal structure. The XRD pattern for the base alloy Zr-9% Nb in Figure 9 (c) shows that the sample contains only β-phase zirconium. The equilibrium phase diagram predicts a dual-phase (α-Zr + β-Nb) microstructure for the Zr-18.7Nb composition at room temperature. However, the XRD in Figure 9 (d) shows that the eutectoid composition alloy sample contains α-phase zirconium and $Zr_{0.883}Nb_{0.117}$ phase. The deviation in phases formed is probably due to the fast-cooling rates after arc-melting used in this study. The pure Zr sample exhibits sharp diffraction peaks characteristic of a monoclinic zirconia (m-ZrO_2) at the surface after oxidation. Whereas the Nb-containing alloys display significantly broader and less intense peaks. This peak broadening may indicate a reduction in crystallite size and a refinement of the oxide microstructure or stresses in the scale. The relationship between these compositional changes and the oxidation kinetics becomes clearer when comparing the 1-hour and 5-day XRD results (Figures 9 (a) to 9 (d)). All 1-hour XRD patterns show strong peaks from the underlying base alloy, such as α-Zr or β-Zr. This base-metal signal simply means that the initial oxide scale formed in Region 1 is still quite thin, allowing X-rays to penetrate it. After 5 days of exposure, these base-alloy peaks disappear.

Looking at the individual compositions, Pure Zr starts with just a few m-ZrO_2 peaks at 1 hour but changes into a thick, coarse m-ZrO_2 layer by day 5. This monoclinic scale fails to protect the underlying metal, matching the rapid degradation and severe microcracking we observed in the post-inflection stage. The hypoeutectoid alloys, on the other hand, suffer from structural instability driven by phase transitions. Over 5 days, the Zr-5Nb scale thickens into a near-complete m-ZrO_2 film at the surface. More importantly, Zr-9Nb forms a thin Zr_3O oxide in early stages of oxidation, in region-1(1-hour exposure), before fully oxidizing into thick m-ZrO_2. Such a phase change likely creates large volume expansions and internal stress, which accounts for the irregular thickening and highly fluctuating kinetic curves seen in Region 2.

In contrast, the eutectoid Zr-18.7Nb behaves differently. It begins with a thin m-ZrO_2 layer but transforms almost completely into a $Nb_{0.8}Zr_{0.2}O_{2.1}$ mixed-oxide phase after 5 days. This phase shift might be the key to its oxidation resistance. The dense $Nb_{0.8}Zr_{0.2}O_{2.1}$ layer acts as a strong diffusion barrier, consistent with the sub-parabolic oxidation behavior observed in Region 2, where the kinetic exponent n_2 is less than 0.3. This can explain the difference in kinetic behaviors before and after the inflection point.

Figures 9 (e) and 9 (f) show the XRD patterns for all tested alloys after oxidation in air at 400°C and 300°C for 5 days, respectively. The main observation from these XRD results is the clear difference in scale thickness compared to the 500°C data discussed above. At 500°C, the 5-day exposure resulted in a thick oxide scale (fully developed m-ZrO_2 or $Nb_{0.8}Zr_{0.2}O_{2.1}$) with no XRD peaks corresponding to the base metal. In contrast, the patterns at 300°C and 400°C still exhibit prominent peaks from the underlying base metal (α-Zr or β-Zr). This persistence of the substrate signal confirms that the oxide scales formed at these lower temperatures remain relatively thin even after 5 days. This microstructural evidence aligns with the kinetics data showing lower weight gains at low temperatures. Additionally, a specific compositional difference was observed at 300°C, where all binary alloys exposed to air showed a distinct NbN peak that was absent in the higher-temperature mature scales.

Oxidation in Steam-Containing Environment

Figure 9 (g) shows the XRD patterns for the oxidation of the all binary-alloy samples after exposure to steam-containing environment at 500°C for 15 days. Comparing the oxides formed under two environments tested at 500°C, the oxide formed in air-environment exhibits m-ZrO_2, Zr_3O, and $Nb_{0.8}Zr_{0.2}O_{2.1}$ which were absent in the oxide formed in steam-containing environment patterns. Whereas the samples exposed to steam-containing environment showed c-ZrO_2, which was absent in the air environment.

Figure 9 (h) and Figure 9 (i) show the XRD patterns for the oxidation of the tested alloy samples exposed to steam-containing environments at 400°C and 300°C for 15 days. Comparing the samples exposed to the two environments at 400°C, the XRD patterns from the air environment are different to those from the steam environment, with the differences being that the steam-containing environment patterns exhibit additional phases such as ω-Zr, ZrH_3, NbN and NbH_2 which are absent in the oxides formed in air-environment.

Additionally, comparing the two environments at 300°C, the steam-containing environment exhibits additional phases such as $NbN_{0.9}O_{0.1}$ and t-ZrO_2 in the surface oxides, which are absent in the oxides formed in equivalent tests in air-environment. At 300°C, the Nb-containing alloys (Zr-5Nb, Zr-9Nb, and Zr-18.7Nb) exposed to air showed a distinct NbN peak, which was absent in the steam-containing environment.

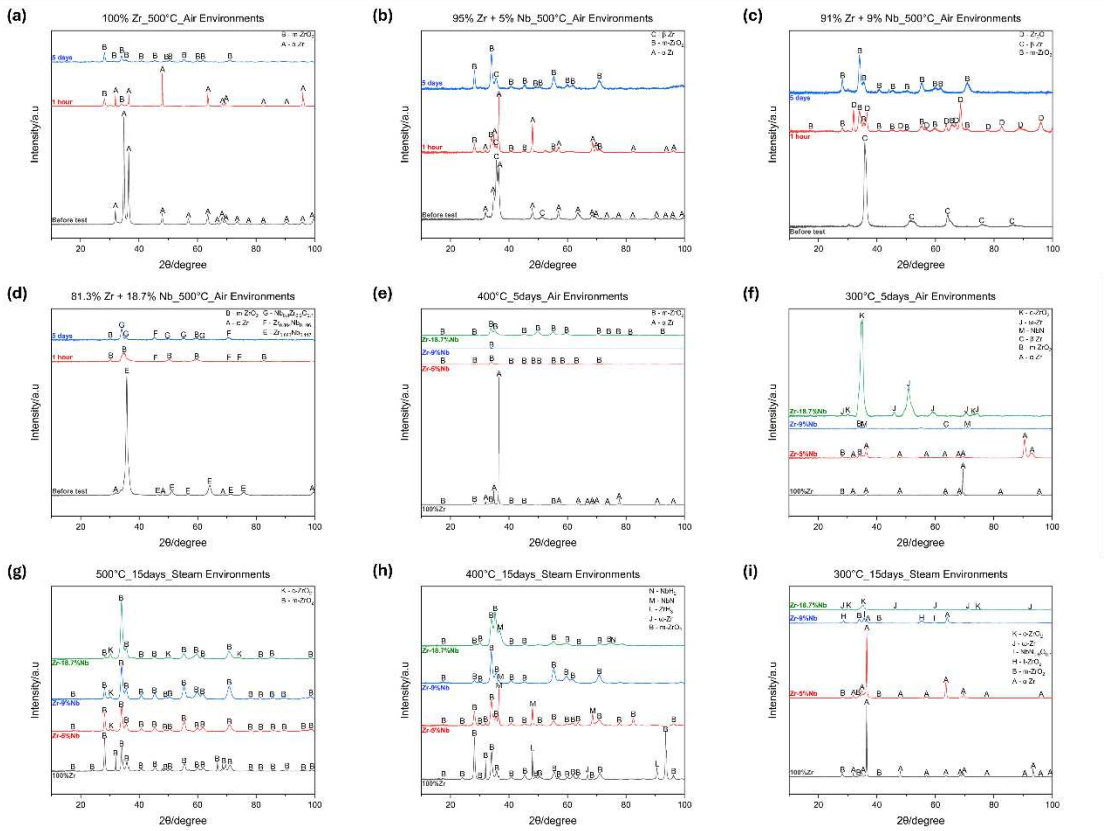

Fig. 9 X-ray diffraction (XRD) patterns collected from the surfaces of pure Zr and Zr–Nb alloys: (a–d) pure Zr, Zr–5% Nb, Zr–9% Nb, and Zr–18.7% Nb, respectively, before oxidation and after oxidation in air at 500 °C for 1 h and 5 days; (e–f) all four materials after oxidation in air for 5 days at (e) 400 °C and (f) 300 °C; and (g–i) all four materials after oxidation in steam-containing environments for 15 days at (g) 500 °C, (h) 400 °C, and (i) 300 °C.

3.8 Post Test Characterization: SEM-EDS Results

Oxidized samples after each test were mounted in epoxy and then sectioned to protect the oxide scale from spalling. Mounted samples were then polished to further characterize scale composition and morphology. The cross-sectional morphologies of the oxide scales formed on the tested alloys after 120 hours of exposure at 500°C in air

are presented in Figures 5 (a) to 5 (d). It should be noted that cross-sectional SEM analysis was exclusively performed on the 500°C samples; the oxidation rates at 300°C and 400°C were too sluggish to produce scales thick enough for accurate cross-sectional morphological evaluation. To provide a clear comparison, the measured scale thicknesses and key microstructural features (such as porosity and microcracking) for all 500°C samples in both air and steam environments are summarized in Table 3.

The oxide scale formed on pure Zr sample exposed to air at 500°C was relatively thick after 120 hours of exposure and showed microcracking, as shown in Figure 5 (a). The oxide scale on Zr-5Nb had some porosity at the outer surface but did not show microcracks or delamination, as shown in Figure 5 (b). Although Zr-9Nb contains higher Nb than the dilute alloys, its oxide morphology reveals structural instability. The scale exhibits irregular thickening and internal stress cracks. The eutectoid sample with Zr-18.7Nb exhibited a uniform, compact, and adherent oxide layer. The interface is sharp and defect-free, and the oxide thickness is noticeably reduced compared to the 5Nb and 9Nb alloys. This dense microstructure effectively provided a better oxidation resistance. The SEM results confirm that the superior oxidation resistance of Zr-18.7Nb stems from its ability to form a compact, crack-free oxide scale.

3.9 SEM Analysis of Steam-Exposed Samples

SEM micrographs of the cross-sectioned samples exposed to the steam-containing environment at 500°C for 168 hours is shown in Figures 10 (a) to 10 (d). Comparison of these micrographs with those for the equivalent samples tested in air, shown in Figures 5 (a) to 5 (d), suggest that the presence of steam in environment has a "densification effect" on hypoeutectoid and eutectoid alloys tested in this study.

The oxide scale formed on pure Zr in steam is continuous, compact, with a reduction in the through-scale porosity and microcracking that characterized the dry-air samples. A similar trend is also observed in Zr-5Nb and Zr-9Nb samples tested in steam-containing environments, where the oxide appears denser and more adherent.

Presence of thin and compact oxides in steam-containing environments implies that steam modifies the defect structure of the oxide. As suggested by Haurais et al. [19] and Buscail et al. [20], the presence of hydroxyl species may relieve growth stresses or enhance sintering at the grain boundaries, promoting the formation of a "barrier-type"

scale that slows down further ionic transport, resulting in a lower oxidation rate despite the aggressive environment.

For the eutectoid Zr-18.7Nb alloy, the aggressive steam environment did not trigger the microcracking and structural breakdown observed in the pure Zr and hypoeutectoid alloys. Instead, as confirmed by the SEM and EDS results, it maintained a thin, compact, and stable mixed-oxide scale, behaving similarly to its performance in dry air.

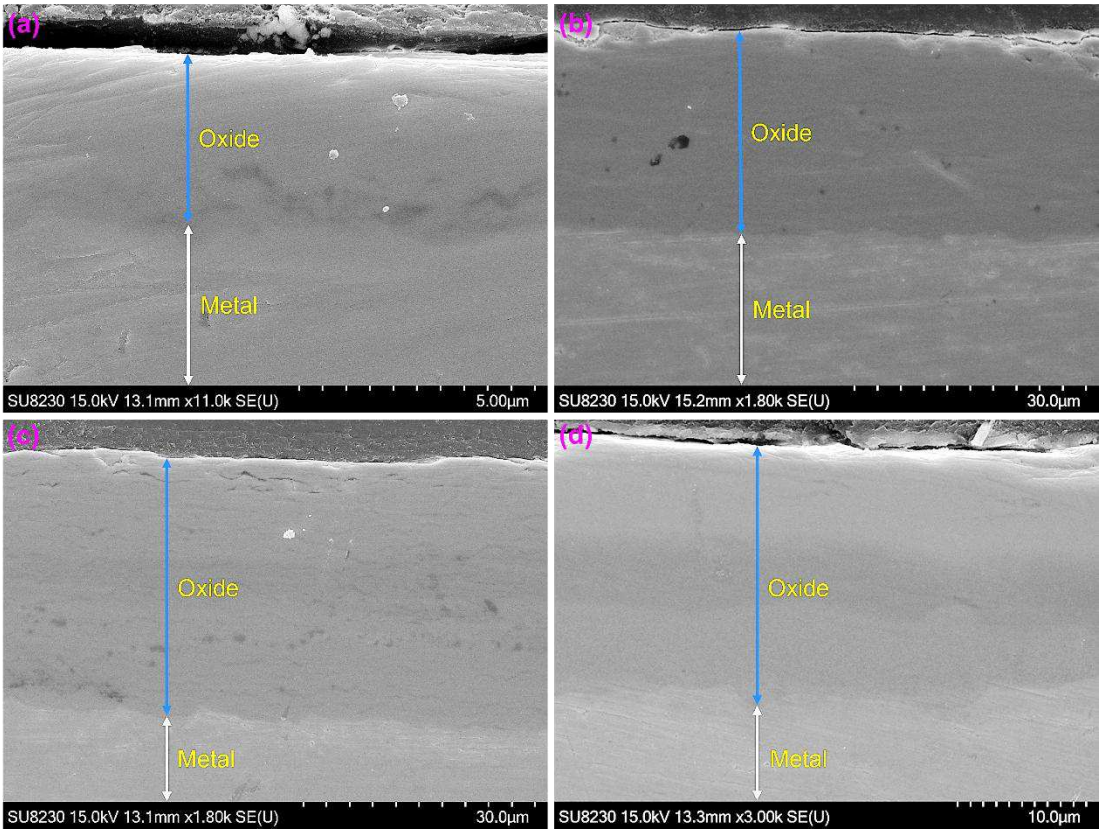

Fig. 10 SEM Micrograph of (a)100% Zr, (b) Zr-5% Nb, (c) Zr-9% Nb, (d) Zr-18.7% Nb alloy samples exposed to steam at 500ºC for 168 hours.

Table 3. Summary of oxide scale thickness and cross-sectional morphology for Zr-Nb alloys exposed to air (5 days) and steam (7 days) at 500°C.

Test Environment	**Alloy**	**Scale Thickness (µm)**	**Morphology & Cracking Observations**
Air (500°C, 5 days)	Pure Zr	30.5	Relatively thick; exhibits severe microcracking and a dual-layer structure.

Air (500°C, 5 days)	Zr-5Nb	31	Some porosity at the outer surface; no obvious microcracks or delamination.
Air (500°C, 5 days)	Zr-9Nb	40	Structural instability; exhibits irregular thickening and internal stress cracks.
Air (500°C, 5 days)	Zr-18.7Nb	19	Uniform, compact, and adherent layer; defect-free interface with reduced thickness.
Steam (500°C, 7 days)	Pure Zr	5	Continuous and compact; reduction in through-scale porosity and microcracking.
Steam (500°C, 7 days)	Zr-5Nb	26.7	Appears denser and more adherent compared to the air-exposed counterpart.
Steam (500°C, 7 days)	Zr-9Nb	35.2	Appears denser and more adherent compared to the air-exposed counterpart.
Steam (500°C, 7 days)	Zr-18.7Nb	23.1	Stable and compact; scale thickness remains similar to the air-exposed sample.

3.10 Composition Profile of Oxide Scales

The elemental distribution across the oxide/metal interface was characterized using EDS line scans to understand the role of Nb incorporation in their oxide. The resulting profiles, presented in Figures 7 (a) to 7 (d), reveal distinct compositional gradients that correlate with the phase stability discussed previously.

For Pure Zr, the EDS profile reveals a dual-layer structure, as shown in Figure 7 (a). The scan distinguishes an outer oxygen-rich region (corresponding to stoichiometric ZrO_2) and an inner, thicker metal-rich region where the oxygen signal gradually diminishes.

Figures 7 (b) and 7 (c) show EDS data for Zr-5Nb and Zr-9Nb respectively. Data shows the critical transition as Nb is introduced into the system.

EDS data shows that the Nb is incorporated in the oxide when Nb is added to Zr, for all hypoeutectoid compositions tested. Crucially, the oxygen profile still shows a gradual decrease into the alloy surface, like Pure Zr, suggesting that the hypoeutectoid Nb content does not fully suppress internal oxidation. This chemical profile, a mix of oxide growth and oxygen dissolution, mirrors the mechanical instability (microcracking) seen in the SEM results. Data in Figures 7 (b) and 7 (c) show that the Nb content increases; the Nb signal within the oxide scale becomes more pronounced and uniform. In Zr-18.7Nb, eutectoid composition, (Figure 7 (d)) the EDS line scans show a uniform distribution of Nb and Zr throughout the oxide scale, with no significant elemental segregation or spikes**.** The transition from the oxide scale to the metal substrate is sharp (step-function like). This implies that the diffusion of oxygen in alloy is effectively arrested at the interface by the chemically stable, mixed-oxide passivation layer, preventing the deep sub-surface oxygen diffusion seen in Pure Zr.

3.11 Chemical Profiling of Steam-Exposed Scales

The EDS line scans for the steam-exposed samples, presented in Figures 11 (a) to 11 (d), provide information on the chemical composition and elemental distribution across the oxide scales formed in the steam-containing environment. These profiles suggest that the "densification effect" of steam alters the oxygen diffusion profile by acting as a stronger barrier against internal oxidation. Specifically, instead of showing a gradual oxygen gradient extending deep into the metallic substrate as observed in dry air, the steam-exposed profiles exhibit a much sharper drop in the oxygen signal at the oxide/metal interface.

Comparing the steam-exposed Pure Zr (Fig. 11 (a)) with its dry-air counterpart (Fig. 7 (a)) reveals a critical difference in oxidation capability. In dry air, Pure Zr exhibited a thick oxide layer with oxygen diffusion extending into the substrate causing internal oxidation. However, in steam (Fig. 11 (a)), the overall oxide thickness is reduced, and the inward flux of oxygen is limited.

The EDS profiles for the hypoeutectoid alloys in steam (Figures 11 (b) and 11 (c)) mirror the densification trend seen in Pure Zr. For the eutectoid sample (Zr-18.7Nb),

the EDS scans confirm that the oxide thickness observed in SEM, as shown in Figure 11 (d) is similar to the scale thickness shown by equivalent data in dry air, Figure 7 (d).

To quantitatively evaluate whether the test environment alters the cation distribution and stoichiometry within the developing scales, the average Zr/Nb ratios across the steady-state plateau of the oxide layers were extracted from the EDS line scans and compared in Fig. 12. As shown in Fig. 12, the measured average Zr/Nb ratios in the oxide scales are 1.86 in air versus 2.04 in steam for Zr-5Nb, 1.56 in air versus 1.88 in steam for Zr-9Nb, and 1.49 in air versus 1.53 in steam for the eutectoid Zr-18.7Nb alloy. Across all compositions, the measured Zr/Nb ratios in the oxide layers are lower than their nominal substrate values, indicating a substantial enrichment of Nb within the growing scale and the incorporation of Nb into complex mixed-oxide phases. Crucially, while a slight increase in the Zr/Nb ratio in steam is observed for the hypoeutectoid alloys (Zr-5Nb and Zr-9Nb), the values between air and steam remain within a comparable quantitative range, and the eutectoid Zr-18.7Nb demonstrates near-identical ratios (1.49 vs. 1.53).

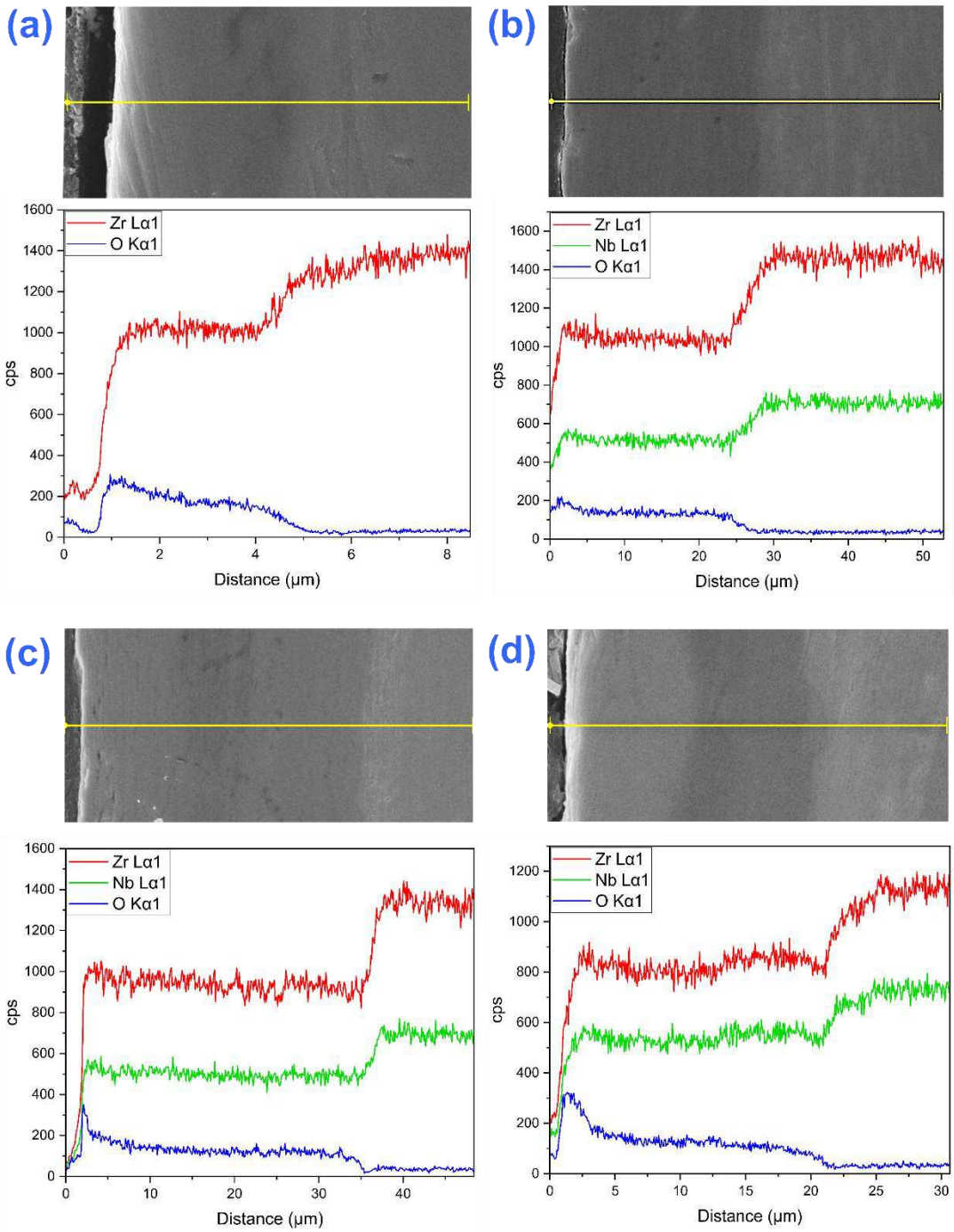

Fig. 11 EDS Line Scan for (a)100% Zr, (b) Zr-5% Nb, (c) Zr-9% Nb, (d) Zr-18.7% Nb alloy samples tested in steam-containing environment for 168 hours at 500 °C.

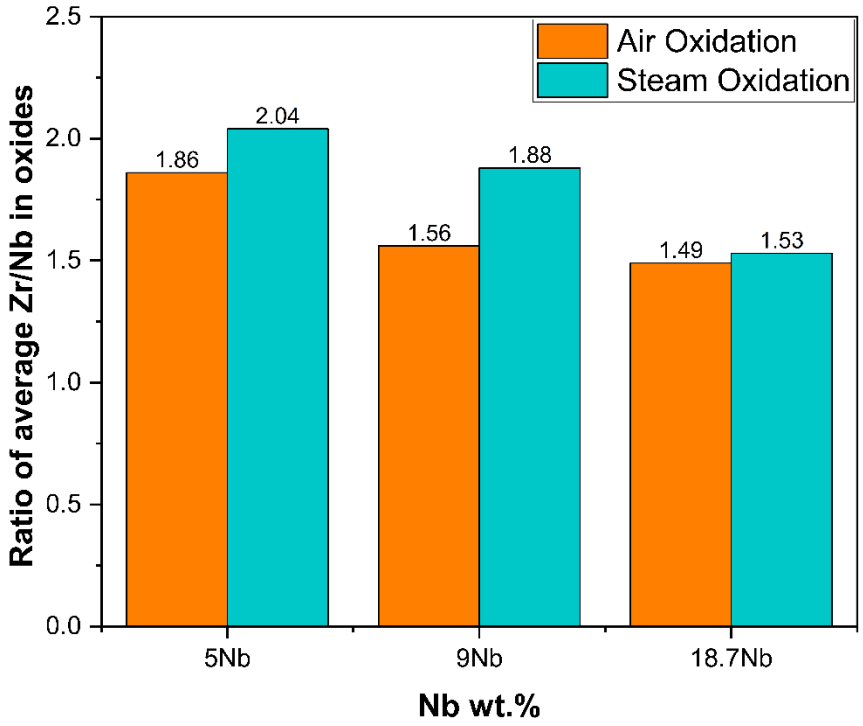

Fig. 12 Zr/Nb EDS intensity ratios obtained from line scans across the oxide scales of Zr–5% Nb, Zr–9% Nb, and Zr–18.7% Nb after exposure at 500 °C to air for 5 days and to a steam-containing environment for 7 days. The ratios were calculated from the Zr and Nb count rates (cps) and represent signal intensity ratios rather than atomic or mass ratios.

4. Discussion

To provide a quantitative assessment of environmental effects, the oxidation rates in terms of oxide thickness, as calculated from cross-sectional SEM images, are summarized in Figure 13. Despite the longer duration in steam environment, a distinct lower growth rate was seen for samples tested in steam-containing environments compared to the ones tested in air.

The most striking contrast was observed in Pure Zr. In dry air, the oxide grew to a thickness of 30.5 μm over 5 days. However, in steam, despite the longer 7-day exposure, the scale thickness dropped dramatically to only 5.0 μm.

As summarized in Figure 13, the steam environment generally reduced the oxidation rate and promoted a more compact oxide layer compared to dry air. Among the tested

alloys, the eutectoid Zr-18.7Nb composition performed the best, maintaining a stable and adherent oxide scale in both air and steam environments across the tested durations.

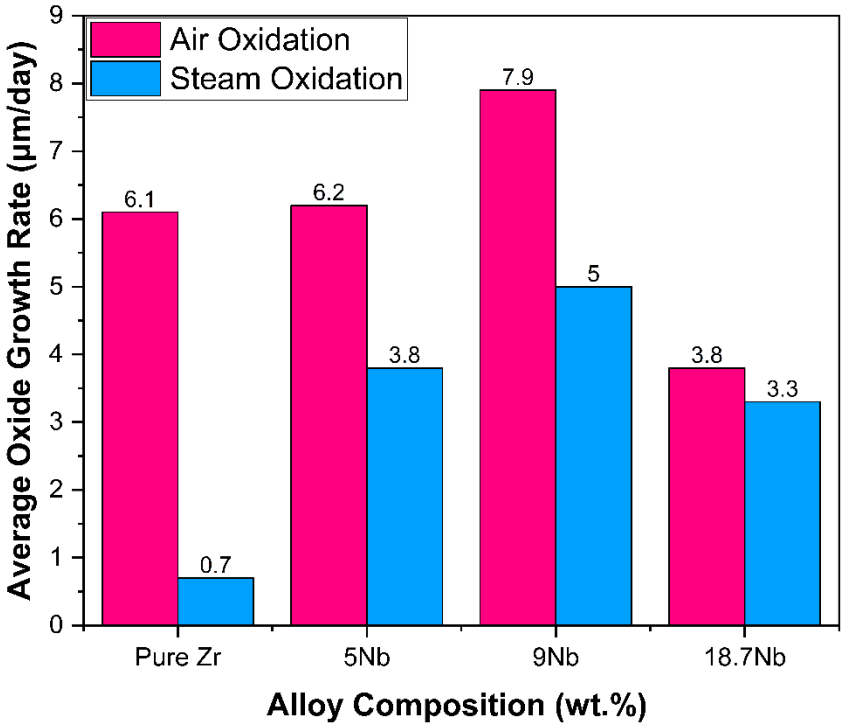

Fig. 13 Average oxide scale growth rates for pure Zr, Zr–5% Nb, Zr–9% Nb, and Zr–18.7% Nb after exposure at 500 °C to air for 5 days and to a steam-containing environment for 7 days. The rates were calculated by dividing the measured oxide scale thickness by the corresponding exposure time.

The oxidation results indicate that the oxidation behavior of Zr-Nb alloys depends on the alloy composition as well as the environmental conditions. A comparison of the corrosion rates, summarized in Figures 14 (a) through 14 (b), highlights distinct differences between dry air and steam environments. In the dry air environment (Figures 14 (a)), the oxidation results exhibit a clear trend where moderate Nb additions consistently enhance resistance.

As shown in the expanded view (Figure 14 (a)), the corrosion rate decreases from ~0.055 mg/cm²/hr (Pure Zr) to ~0.035 mg/cm²/hr (Zr-18.7Nb). This improvement can be fundamentally explained by the "Doping Effect" through defect chemistry. In the monoclinic zirconia lattice, oxygen diffusion is primarily governed by the migration of

oxygen vacancies ($V_O^{\cdot\cdot}$). When pentavalent niobium ions (Nb^{5+}) substitute for tetravalent zirconium ions (Zr^{4+}), they create substitution defects with a relative positive charge ($Nb_{Zr}^{\cdot}$). To maintain overall electroneutrality within the lattice, this substitution process must be compensated for by the consumption of pre-existing oxygen vacancies. The schematic Kröger-Vink reaction describing oxygen-vacancy consumption is given in Equation 1.

According to Equation 1, the incorporation of Nb directly annihilates the oxygen vacancies ($V_O^{\cdot\cdot}$) and creates regular oxygen lattice sites ($O_O^{\times}$). Since these oxygen vacancies act as the primary pathways for inward oxygen diffusion through the oxide scale, their suppressed concentration significantly restricts the oxygen transport, thereby slowing down the parabolic growth rate and stabilizing the protective tetragonal oxide phase [21, 22].

In contrast to the dry air results, the steam environment (Figure 14 (b)) shows a different effect of Nb addition on the intrinsic oxidation resistance of the zirconia scale. Pure Zr in the steam-containing environment showed a very low oxidation rate of ~0.003 mg/cm²/hr**.** The Zr-9Nb alloy exhibited the poorest performance among the four samples, peaking at ~0.025 mg/cm²/hr. While the eutectoid composition, Zr-18.7Nb, also showed a lower oxidation rate of (~0.016 mg/cm²/hr).

A general comparison between the results reveals a fundamental difference in the role of Niobium depending on the oxidant. For Pure Zr, the oxidation rate in steam (~0.003 mg/cm²/hr) is approximately 18 times lower than in air (~0.055 mg/cm²/hr). This kinetic data is corroborated by the oxide scale thickness measurements (Table 3), where the scale on Pure Zr was significantly thinner in steam (~5 μm) than in air (~30.5 μm). It is critical to address the apparent inconsistency between the weight-gain-derived corrosion rates in Figure 14 (a) and the physical oxide scale thicknesses in Table 3, particularly regarding Pure Zr and Zr-9% Nb. In Figure 14 (a), Pure Zr exhibits the highest corrosion rate, yet its physical oxide thickness in Table 3 (~30.5 μm) is lower than that of Zr-9% Nb. This discrepancy is fundamentally resolved by examining the continuous TGA data-logging method and the physical phenomenon of scale spallation. The corrosion rates in Figure 14 (a) were calculated using the maximum weight registered continuously by the computer over the 120 hours exposure. For Pure Zr, the oxidation reaction is aggressive, leading to a rapid and higher oxygen weight gain

(hence the highest peak weight and calculated corrosion rate). However, due to the high growth stresses and severe through-scale microcracking of the un-stabilized monoclinic zirconia (m-ZrO_2), significant scale spallation was seen on pure Zr sample during the latter stages of exposure in air. Because the corrosion rate calculation utilizes the peak weight prior to major mass loss events, it accurately captures the higher chemical reaction kinetics. Conversely, when preparing the cross-sections for SEM characterization (Figure 5), these spalled oxide fragments were physically detached, leaving only the remaining adhered inner scale to be measured. In contrast, the Zr-9% Nb alloy exhibits a lower chemical weight gain (lower peak weight in Figure 14 (a)) but forms a cracked and volumetrically expanded oxide scale due to local phase instabilities. Because this bulk scale remains largely attached to the substrate without complete exfoliation, the SEM cross-section captures its bulky physical thickness, making it appear thicker than the partially spalled Pure Zr scale. Therefore, the apparent mismatch is a combined artifact of peak-weight TGA data filtering and physical scale exfoliation during high-temperature exposure. This improvement is fundamentally attributed to the steam-induced scale densification effect discussed earlier in Section 3.9.

The fundamentally different role of Nb in the steam environment can be attributed to the introduction of hydrogen species from water dissociation. In dry air, Nb acts as a beneficial oxygen vacancy suppressor. However, in steam, our XRD results (discussed in Section 3.7) revealed the formation of distinct hydride phases, such as ZrH_3 and NbH_2. For the Nb-containing alloys, particularly the metastable hypoeutectoid Zr-9Nb, the precipitation of these hydrides likely induces volumetric expansion and internal localized stresses. This hydrogen-induced structural instability counteracts the beneficial densification effect that normally occurs in steam. As a result, the protective scale is partially disrupted by these internal stresses, creating new short-circuit diffusion paths. This mechanism explains why Pure Zr, which benefits from steam-induced densification without the severe disruptive complications of Nb-hydride precipitation, offers the best intrinsic oxidation resistance in the steam environment.

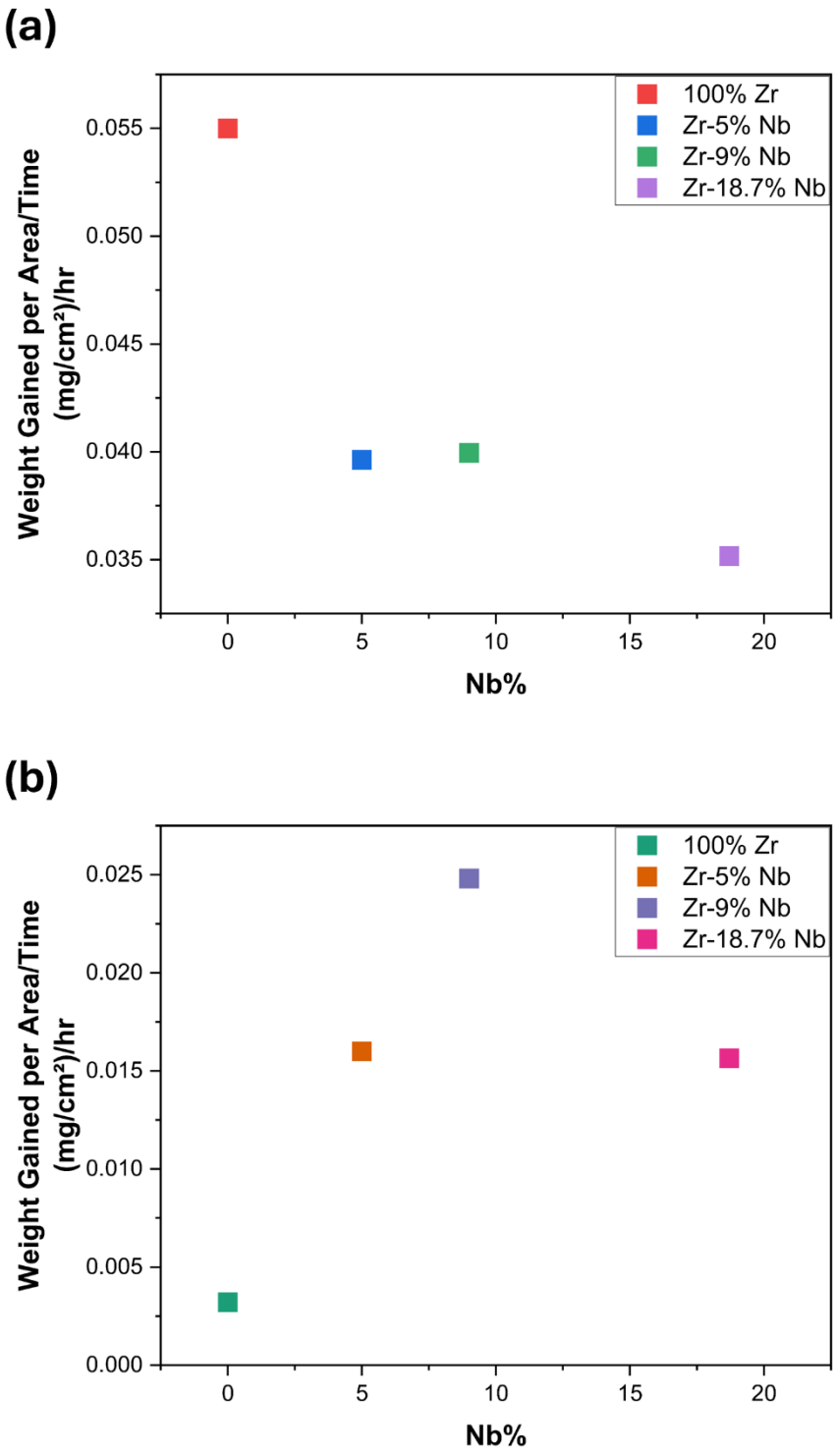

Fig. 14 Mass-gain-based oxidation rates of pure Zr, Zr–5% Nb, Zr–9% Nb, and Zr–18.7% Nb at 500 °C in (a) dry air and (b) a steam-containing environment. Rates were calculated by dividing the maximum mass gain per unit area recorded during 120 h by 120 h for (a), and the mass gain per unit area measured after 168 h by 168 h for (b).

The kinetic data extracted from the initial oxidation stage demonstrate that niobium modifies the fundamental transport mechanisms in zirconia formed on these Zr-Nb alloys. The activation energy for pure Zr (124.6 kJ/mol) aligns closely with the enthalpy of oxygen vacancy migration [17], indicating that early-stage oxidation is dominated by short-circuit diffusion along grain boundaries without the need for additional vacancy formation energy. When a moderate amount of Nb is added (Zr-5Nb), the activation energy sharply increases to 242 kJ/mol (Table 2). This kinetic shift is driven by the defect chemistry due to doping effect. As pentavalent Nb substitutes for tetravalent Zr, pre-existing oxygen vacancies are consumed to maintain electroneutrality (see Equation 1) [13]. Because oxygen vacancies are the primary diffusing species, their suppression limits inward oxygen transport and raises the overall energy barrier for oxidation. For Zr-9Nb, the lower apparent activation energy and irregular scale growth may reflect contributions from both microstructural instability and changes in oxide defect chemistry. As discussed in the Introduction, Nb incorporation can increase the Zr vacancy concentration in tetragonal ZrO_2 under oxygen-rich conditions [13], potentially facilitating outward Zr transport. However, the present data do not establish the relative contributions of cation transport and microstructural degradation to the observed oxidation behavior.

A direct comparison between air and steam exposures reveals a distinct bifurcation in how these environments interact with the oxide scale. For pure Zr, the steam environment acts as a strong passivating agent. The presence of hydroxyl species likely facilitates stress relaxation and enhances grain boundary sintering, leading to a massive densification effect [19, 20]. This mechanism explains why the scale thickness of pure Zr dropped from 30.5 μm in air to just 5.0 μm in steam at 500°C (Table 3). Conversely, this steam-induced densification is severely disrupted in hypoeutectoid alloys (Zr-5Nb and Zr-9Nb). The XRD analysis provides the physical explanation for this disruption: the detection of distinct hydride phases (ZrH_3 and NbH_2) unique to the steam environment (Fig. 9 (h)). The precipitation of these hydrides near the metal-oxide interface generates localized volumetric expansion and internal stress. This hydrogen-induced physical damage physically fractures the scale, creating short-circuit diffusion paths that counteract the beneficial hydroxyl sintering effect.

A quantitative comparison of the EDS line scans (Fig. 12) provides critical insight into the relationship between oxide chemistry and environmental degradation. The

measured Zr/Nb ratios in the oxide scales range from ~1.49 to ~2.04 across both air and steam exposures. The substantial departure from the nominal bulk metal ratios demonstrates that Nb cations segregate and enrich extensively within the growing scale, participating in the formation of protective mixed-oxide phases such as $Nb_{0.8}Zr_{0.2}O_{2.1}$. More importantly, examining the environmental effect reveals that the overall cation stoichiometry is relatively stable between dry air and steam (1.86 vs. 2.04 for Zr-5Nb, 1.56 vs. 1.88 for Zr-9Nb, and 1.49 vs. 1.53 for Zr-18.7Nb). The fact that the average oxide composition does not undergo a radical shift confirms that the profound divergence in oxidation rates between air and steam cannot be driven by macroscopic composition alterations. Instead, the dramatic acceleration of corrosion in hypoeutectoid alloys (Zr-5Nb and Zr-9Nb) in steam is governed by microstructural destabilization, specifically, the dissociation of water leading to the precipitation of brittle hydride phases (ZrH_3 and NbH_2) and subsequent scale microcracking. Conversely, the eutectoid Zr-18.7Nb maintains near-identical Zr/Nb ratios (1.49 vs. 1.53) and superior kinetic resistance in both atmospheres, validating the exceptional chemical and mechanical stability of its mixed-oxide barrier.

The experimental results ultimately establish that bulk phase stability dictates long-term protectiveness. The eutectoid Zr-18.7Nb alloy maintained exceptional oxidation resistance across all tested temperatures and environments. Unlike pure Zr, which degraded into a porous monoclinic oxide, or Zr-9Nb, which suffered from sub-oxide transitions, Zr-18.7Nb quickly formed a uniform and adherent $Nb_{0.8}Zr_{0.2}O_{2.1}$ mixed-oxide phase (Fig. 9 (d)). EDS profiling confirmed that this stable mixed-oxide layer sharply halted the inward diffusion of oxygen (Fig. 7 (d) and Fig. 11 (d)), preventing the deep substrate penetration observed in the other alloys. This stable structural arrangement allowed Zr-18.7Nb to maintain a highly protective sub-parabolic kinetic regime ($n_2<0.3$, Fig. 4 (b)), proving that matching the alloy composition to a stable multi-component oxide phase is the most effective strategy for mitigating high-temperature corrosion.

5. Conclusions

The oxidation behavior of Zr-Nb alloys ranging from pure Zr to the eutectoid composition (18.7 wt.% Nb) was systematically evaluated at 300°C–500°C in dry air and steam. The primary findings are summarized as follows:

1. The addition of Nb alters the initial energy barrier for oxidation. Minor Nb additions (Zr-5Nb) nearly double the activation energy (from 124.6 kJ/mol to 242.0 kJ/mol) by consuming oxygen vacancies through the Kröger-Vink substitution mechanism. However, structural instability at higher, non-eutectoid Nb levels (Zr-9Nb) negates this chemical benefit.

2. Pure Zr exhibits poor resistance in dry air due to rapid monoclinic scale cracking but shows excellent resistance in steam-containing environments due to hydroxyl-driven scale densification (achieving an 18-fold reduction in oxidation rate).

3. While steam improves the pure Zr scale, it acts as a destabilizer for intermediate Nb alloys. The formation of ZrH_3 and NbH_2 hydride phases in steam induces internal stresses and volumetric expansion, causing microcracking that destroys the protective barrier in Zr-5Nb and Zr-9Nb.

4. Quantitative EDS profiling demonstrates that Nb enriches within the oxide scales, resulting in average Zr/Nb ratios ranging between 1.49 and 2.04 across all tested alloys. The testing atmosphere does not fundamentally disrupt this cation distribution, showing only a modest shift from 1.86 to 2.04 for Zr-5Nb and 1.56 to 1.88 for Zr-9Nb, while remaining virtually invariant for Zr-18.7Nb (1.49 in air vs. 1.53 in steam). This demonstrates that the drastic kinetic divergence between air and steam environments is governed by defect-level phenomena and localized hydride-induced microcracking rather than macroscopic alterations in oxide cation stoichiometry.

5. The Zr-18.7Nb eutectoid alloy provides the best oxidation resistance in both air and steam-containing environments. By forming a dense, chemically stable $Nb_{0.8}Zr_{0.2}O_{2.1}$ mixed-oxide phase, it successfully arrests deep oxygen diffusion and avoids both the microcracking seen in air and the hydride-induced breakdown seen in steam, maintaining a protective sub-parabolic growth rate ($n_2<0.3$).

Competing Interests

The authors declare that they have no competing interests.

Data Availability Statement

The data supporting the findings of this study are available from the corresponding author upon reasonable request.

Author Contributions

Sean Li: Methodology, Investigation, Formal analysis, Writing – original draft. Chaitanya S. Deo: Analysis, Writing – review & editing, Funding acquisition, Visualization, Project administration. Remi Dingreville: Writing – review & editing. Scott Monismith: Validation, Conceptualization. Preet M. Singh: Supervision, Analysis, Writing – review & editing, Funding acquisition.

Funding/Acknowledgments

The authors acknowledge support from the Department of Homeland Security Nuclear Forensics office. This work was supported in part by the Center for Integrated Nanotechnologies, an Office of Science user facility operated for the U.S. Department of Energy.

This article has been authored by an employee of National Technology & Engineering Solutions of Sandia, LLC under Contract No. DE-NA0003525 with the U.S. Department of Energy (DOE). The employee owns all right, title, and interest in and to the article and is solely responsible for its contents. The United States Government retains and the publisher, by accepting the article for publication, acknowledges that the United States Government retains a non-exclusive, paid-up, irrevocable, world-wide license to publish or reproduce the published form of this article or allow others to do so, for United States Government purposes. The DOE will provide public access to these results of federally sponsored research in accordance with the DOE Public Access Plan (https://www.energy.gov/downloads/doe-public-access-plan).

The authors thank Jamshad Mahmood of the Renewable Bioproducts Institute at the Georgia Institute of Technology for assistance with the experimental setup. The authors also thank Tanner Rydalch of the George W. Woodruff School of Mechanical Engineering at the Georgia Institute of Technology and Nathan Bianco of Sandia National Laboratories for assistance with data collection.

References

[1] Rosa CJ. Oxidation of zirconium—A critical review of literature. J Less Common Met. 1968;16:173–201.

[2] Banerjee S, Mukhopadhyay P. Phase Transformations: Examples from Titanium and Zirconium Alloys. Vol. 12. Burlington, MA: Elsevier Science; 2010.

[3] Vandegrift JL, Price PM, Stroud JP, et al. Oxidation behavior of Zirconium, Zircaloy-3, Zircaloy-4, Zr-1Nb, and Zr-2.5 Nb in air and oxygen. Nucl Mater Energy. 2019;20:100692.

[4] Motta AT, Couet A, Comstock RJ. Corrosion of zirconium alloys used for nuclear fuel cladding. Annu Rev Mater Res. 2015;45:311–343.

[5] Steinbrueck M, da Silva FO, Grosse M. Oxidation of Zircaloy-4 in steam-nitrogen mixtures at 600–1200 °C. J Nucl Mater. 2017;490:226–237.

[6] Khanna AS. Introduction to High Temperature Oxidation and Corrosion. Materials Park, OH: ASM International; 2002.

[7] Steinbrück M. Prototypical experiments relating to air oxidation of Zircaloy-4 at high temperatures. J Nucl Mater. 2009;392:531–544.

[8] Elshanshoury IA, Rudenko VA, El-Dahshan ME, Hammad FH. Kinetics of oxidation of Zr-1%Nb alloy in pressurized steam and air at 400–700 °C. Corros Sci. 1969;9:217–224.

[9] Roy SP, Gupta NK, Mukerjee SK, Parida SC. Oxidation kinetics of Zr-Nb alloys in dry air in the temperature range 723–790 K. Indian J Adv Chem Sci. 2017;5:255–262.

[10] Arima T, Miyata K, Idemitsu K, Inagaki Y. Oxidation properties of Zr–Nb alloys at 973–1273 K in air. Prog Nucl Energy. 2009;51:307–312.

[11] Jeong YH, Lee KO, Kim HG. Correlation between microstructure and corrosion behavior of Zr–Nb binary alloy. J Nucl Mater. 2002;302:9–19.

[12] Kim HG, Park SY, Lee MH, Jeong YH, Kim SD. Corrosion and microstructural characteristics of Zr–Nb alloys with different Nb contents. J Nucl Mater. 2008;373:429–432.

[13] Otgonbaatar U, Ma W, Youssef M, Yildiz B. Effect of niobium on the defect chemistry and oxidation kinetics of tetragonal ZrO_2. J Phys Chem C. 2014;118:20122–20131.

[14] Huang J, Pei W, Xu S, et al. Degradation mechanism on corrosion resistance of high Nb-containing zirconium alloys in oxygen-containing steam. Acta Metall Sin. 2024;60:509–521.

[15] Parida SC, Gupta NK, Krishnan K, Rama Rao GA, Sen BK. High-temperature oxidation of β-NbTi alloys. Metall Mater Trans A. 2008;39:2020–2025.

[16] Sun Y, Li K, Gao B, et al. Study on microstructure and wear resistance of Zr-17Nb alloy irradiated by high current pulsed electron beam. Rev Adv Mater Sci. 2020;59:514–522.

[17] Madeyski A, Smeltzer WW. Oxygen diffusion in monoclinic zirconia. Mater Res Bull. 1968;3:369–375.

[18] Swaroop S, Kilo M, Argirusis C, Borchardt G, Chokshi AH. Lattice and grain boundary diffusion of cations in 3YTZ analyzed using SIMS. Acta Mater. 2005;53:4975–4985.

[19] Haurais F, Beuzet E, Steinbrück M, et al. Porosimetry of ZrO_2 scales formed during oxidation of Zr-based fuel claddings in nuclear severe accident conditions. In: Proceedings of the 24th International Conference Nuclear Energy for New Europe (NENE 2015); September 14–17, 2015; Portorož, Slovenia. 2015. Paper

805.

[20] Buscail H, Rolland R, Issartel C, Perrier S, Latu-Romain L. Stress determination by in situ X-ray diffraction–Influence of water vapour on the Zircaloy-4 oxidation at high temperature. Corros Sci. 2018;134:38–48.

[21] Couet A, Motta AT, Ambard A. The coupled current charge compensation model for zirconium alloy fuel cladding oxidation: I. Parabolic oxidation of zirconium alloys. Corros Sci. 2015;100:73–84.

[22] Yan K, Carr DG, Kabra S, et al. In situ characterization of lattice structure evolution during phase transformation of Zr-2.5 Nb. Adv Eng Mater. 2011;13:882–886.